Journal of South American Earth Sciences
January 2024, Volume 133, Pages 104700 (24p.)
https://doi.org/10.1016/j.jsames.2023.104700 https://archimer.ifremer.fr/doc/00861/97314/

New constraints on the Late Miocene-Pliocene deformational and depositional evolution of the Eastern Cordillera and Sub-Andean Zone in Southern Peru

Moizinho G.R. [1, 2, 3, *], Roddaz M. [1], Brichau S. [1], Louterbach M. [4], Dantas E.L. [2], Santos R.V. [2], Bayon Germain [3], Vink J. [5], Hoorn C. [6, 7]

[1] Géosciences-Environnement Toulouse, Université de Toulouse, Toulouse, France
[2] Instituto de Geociências, Universidade de Brasília, Brasília, Brazil
[3] IFREMER, Geo-ocean, Plouzané, France
[4] Harvard Graduate School of Design, Department of Landscape Architecture, Cambridge, USA
[5] Bassins-Réservoirs-Ressources, Institut Polytechnique Lasalle Beauvais, Beauvais Cedex, France
[6] Centre for Biodiscovery School of Biological Sciences Victoria University of Wellington Wellington, New Zealand
[7] Institute of Biodiversity and Ecossistem Dynamics, University of Amsterdam, Netherlands

* Corresponding author : G. R. Moizinho, email address : gabriel.ribeiro-moizinho@univ.tlse3.fr

Abstract :

The deformation history of the Eastern Cordillera (EC) and Sub-Andean Zone (SAZ) of southern Peru is critical for understanding the roles that tectonics and climate played in the erosional exhumation of bedrock and the associated sediment flux delivered to the Amazon drainage basin. In this study, we report new field and subsurface data, apatite fission track (AFT) and (U–Th)/He thermochronological ages, U–Pb ages on detrital zircon grains, Sr–Nd isotopic compositions of fine sediments, which combined with previously published data, provide new constraints on the Neogene deformation and deposition history across the southern Peruvian EC and SAZ between 12° and 14°S. Late Miocene-Pliocene deformation is recorded by AFT and AHe ages in both the EC and SAZ and by growth strata geometry in the SAZ. This period is characterized by the development of piggy-back synclines and duplexes in the SAZ, overthrusting of the EC, and input of recycled sedimentary rocks of the SAZ and first cycle sediments from Triassic Plutonic rocks from the EC to the late Miocene-Pleistocene piggy-back syncline sediments. We report a transition from low-energy sand-dominated to high-energy conglomerate-dominated deposits in the Plio-Pleistocene marking an increase in sedimentation rates, indicating that the thrust wedge has continued to propagate. Our data agrees with that of previously published studies and indicate that the Late Miocene-Pliocene was a period of tectonic uplift and deformation in both the EC and SAZ.

Highlights

► Timing of Late Miocene-Pliocene uplift of the Eastern Cordillera and Sub Andean Zone constrained by AFT and AHe data. ► Transition from a low to high energy fluvial system in the Late Miocene-Pliocene. ► Provenance analysis of the Madre de Dios basin indicates Eastern Cordillera denudation and recycling of SAZ sediments.

Keywords : Andes, Miocene-Pliocene, Uplift, Thermochronology, Chronostratigraphy, Provenance

1. Introduction

The Andes, the longest and second largest continental mountain range on Earth, constitute an important barrier to atmospheric fluxes in the Southern Hemisphere and affect the regional-scale climate by blocking zonal flows, influencing regional wind patterns, and precipitation rates (Figure 1; Lenters and Cook, 1995; Campetella and Vera, 2002; Garreaud et al., 2003; Insel et al., 2010; Espinoza et al., 2020). Hence, the rise of the Andes is thought to have affected the climate in the eastern Pacific Ocean, besides moisture transport, and precipitation patterns in the adjacent Amazon Basin (Uba et al., 2007; Sepulchre et al., 2009; Insel et al., 2010; Poulsen et al., 2010).

The Eastern Cordillera (EC) and the Sub-Andean Zone (SAZ) define the Eastern Andean Orogenic wedge of Bolivia and Peru and constitute an orographic barrier to the moisture flux from the Amazon (e.g., Bookhagen and Strecker, 2008; Chavez and Takahashi, 2017). Most of the studies indicate that the EC experienced deformation, exhumation, and surface uplift during the Miocene (e.g., Horton, 1999; McQuarrie et al., 2008b; Eude et al., 2015; Sundell et al., 2019). In Bolivia, by comparing the shape of the wedge assimilated to a Coulomb wedge and the present climatic zones, Horton (1999) interpreted precipitation-induced erosion to be responsible for a lesser propagation of the wedge in the north. Similarly, the decrease in width of the northern Bolivian Eastern Orogenic wedge has been interpreted as the result of a wetter climate of northern Bolivia since ca. 19 Ma (McQuarrie et al., 2008b). Alternatively, weakening of the retroarc lithosphere and development of a crustal-scale detachment due to strain accumulation in the Central Andes (13-22°C; Oncken et al., 2012) as well as inherited properties of the retroarc lithosphere or flat slab subduction (Horton et al., 2022) may explain accelerated shortening in the SAZ since the Middle Miocene.

The SAZ defines the eastern limit of the Central Andes, and it provides an example of an active fold and thrust belt in a retro-arc, non-collisional setting (Figure 2). The onset of the SAZ deformation of the Central Andes and its Neogene history varies. Pliocene thrusting and forward propagation of the deformation has been documented in the SAZ in central and northern Peru (4-12.5 Lat S°, Espurt et al., 2011; Gautheron et al., 2013; Eude et al., 2015). However, in northern Bolivia and southern Peru (12.5-17 Lat S°), the absence of deformation in the EC and a “limited deformation in the Subandes” for the past 4 Ma in northern Bolivia and southern Peru have been used to advocate for a Pliocene climatic control on the exhumation and erosion of the terrain, (Lease and Ehlers, 2013).

In this paper, we revisited the Late Miocene-Pliocene exhumation history of the Amazonian southern Peruvian SAZ based on the correlation of previously published seismic sections (Baby et al., 2018b; Zamora et al., 2019), thermochronology (Mora et al., 2011; Baby et al., 2018b) and biostratigraphic ages (Marivaux et al., 2012; Antoine et al., 2013) with new AFT and AHe ages. Additionally, we report new sedimentological, provenance (Sr-Nd isotopic compositions of fine sediments and U-

Pb ages of detrital zircon in sandstones), biostratigraphic and chronostratigraphic ($^{40}Ar/^{39}Ar$ in biotite ages) data sets to better understand the basin-fill evolution of the Madre de Dios retroarc foreland basin in response to the forward propagation of the Eastern Andean Orogenic wedge.

2. Geological Background

2.1 Structural setting

The studied area is located between 12º and 14º S latitudes on the eastern side of the Peruvian Andes, and it comprises the EC and the Madre de Dios Basin. The basin is part of the southern Amazonian foreland basin systems and can be divided into the SAZ and the Madre de Dios foredeep (Gil, 2001; Hermoza, 2004; Roddaz et al., 2005b; Figure 2). The Madre de Dios basin is bounded in the southwest by the Azulmayo thrust, which places pre-Mesozoic rocks of the EC over the Mesozoic sedimentary rocks of the SAZ, north and northeast by the Brazilian Shield, and north and northwest by the Fitzcarrald Arch. The southern Peruvian EC is a double verging thrust wedge consisting, in its inner part, of an SW-verging system of thrust faults and folds of the Central Andean back thrust belt involving Paleozoic and Mesozoic sedimentary strata (McQuarrie and DeCelles, 2001). In its outer part, Permo-Triassic plutons and metamorphosed Precambrian and Paleozoic strata (Dalmayrac et al., 1980; Kontak et al., 1990; Mišković et al., 2009) overthrusting the SAZ. The oldest rocks outcropping in the studied area are the metamorphic rocks of the “Iscaybamba Complex”. The exact age of these metamorphic rocks is unknown, but they could be Cambrian or older (Marocco, 1978; Megard, 1978; Dalmayrac et al., 1980; Dalmayrac and Molnar, 1981; Laubacher, Gérard and Megard, 1985). In this section (see location in Figure 3), the EC is interpreted as a large crustal-scale ramp anticline above a footwall ramp. Additional east-verging faults to the west of the anticline are interpreted to repeat the Ordovician section (i.e., Marcapata and Ollachea thrust faults, Figures 2 and 3).

In the Madre de Dios Basin, the SAZ is separated from the EC by the Azulmayo thrust, also known as the “Main thrust” (Perez et al. 2016), and from the foredeep by the Tambopata thrust, which corresponds to the Sub-Andean thrust front (Figures 3 and 4). The SAZ is interpreted as being constituted of a hinterland dipping duplex developed either in the Paleogene sedimentary infill (Figure 4, Baby et al., 2018b; Gil Rodriguez et al., 2001) or in the Ordovician to Cretaceous series (Perez et al., 2016).

On the other hand, Mora et al. (2014) have interpreted it as a thin-skinned passive-roof duplex. This duplex is overthrust by an imbricate system of Cretaceous strata as observed in seismic lines (see Figure 17B in Baby et al., 2018b), and field relationships (see Figure 18 in Baby et al. 2018b and Figure 38 in Louterbach, 2014). The propagation of the deformation towards the Madre de Dios foredeep is partly controlled by the development of the deep duplexes. Their shortening is accommodated at the surface by tectonic imbricates and by the Tambopata frontal thrust (Gil Rodriguez et al., 2001; Baby et al., 2018a), which transported eastwards the Punquiri piggyback syncline consisting of Cenozoic sediments (Baby et al., 2018a). The strata involved in the Punquiri syncline are Paleogene through to Plio-Pleistocene in age, as shown by biostratigraphic evidence (Antoine et al., 2013; Louterbach et al., 2014; this study).

The balanced cross-section published by Baby et al. (2018b) shows that the shortening in the SAZ is kinematically linked to the displacement of the EC over a crustal-scale ramp, linking the development of the EC crustal anticline to the documented shortening in the SAZ. This link has also been recognized in other parts of the eastern Andes (Echavarria et al., 2003; Espurt et al., 2011; Eude et al., 2015). Since this transport of the EC along a crustal ramp implies a tectonic uplift, it follows that it was also contemporary with the deformation of the SAZ.

2.2. Neogene Stratigraphic Framework

The Madre de Dios Basin sedimentary infill consists of approximately 3.3km of siliciclastic sediments that overlie the marine Cretaceous Cachiayacu Formation. Its stratigraphic record has been described regarding both the SAZ and foredeep compartments (Gil Rodriguez, 2001; Hermoza, 2004; Roddaz et al, 2010). In the SAZ, three units are recognized: the Paleocene Huayabamba Formation, the Miocene Ipururo Group, and the Plio-Pleistocene Mazuko Formation. In the foredeep, the two older units are also observed, and the Plio-Pleistocene Mazuko Formation absent. These depositional ages are supported by palynological data (Carpenter and Berumen, 1999; Cooperación Técnica Peruana-Alemana, 1982; Gutierrez, 1982; Valdivia, 1974), thermochronological analysis (Apatite to Zircon Inc., 2004; Hermoza, 2004) and radiometry ($^{40}Ar/^{39}Ar$ on volcanic feldspar and biotite; Campbell et al., 2001; Gil Rodriguez, 2001; Mobil Oil Corporation, 1998).

In the SAZ, the Ipururo Group consists of Miocene deposits divided into three formations: the Bala, Quendeque, and Charqui formations (Roddaz et al., 2010). At first, these formations were thought to be fluvial to alluvial in nature (Gil Rodriguez, 2001; Hermoza, 2004; Roddaz et al., 2010). Alluvial, deltaic, and estuarine coastal plain facies have been reported in the Miocene Bolivian Quendeque Formation (Hovikoski et al., 2007b; Hovikoski et al., 2007c). Miocene tidal-influenced deposits were also described in the Bolivian Beni-Mamoré Basin, which is adjacent to the Madre de Dios Basin (Roddaz et al., 2006).

In the Peruvian foredeep, the Ipururo Group encompasses the Ipururo Formation and Units A and B of the Madre de Dios Formation (Campbell et al., 2001). The Ipururo Formation is thought to be Miocene in age based on stratigraphic correlations (Hermoza, 2004). The Madre de Dios Formation is Late Miocene ($^{40}Ar/^{39}Ar$ dating on feldspars at 9.01 ± 0.28 Ma, Campbell et al. 2001) and thus considered as a lateral equivalent of the Bolivian Charqui Formation (Roddaz et al., 2010). Overall, the Madre de Dios Formation has been interpreted as formed by tide-dominated estuarine deposits (Hovikoski et al., 2005; Roddaz et al., 2006).

3. Sampling and methodologies

3.1. Low temperature thermochronology

Eight samples were collected along two vertical profiles in the eastern flank of the EC for Apatite Fission Track (AFT) and Apatite U-Th/He (AHe) analyses: six Permo-Triassic plutonic rocks (MD164, MD169, MD170, MD192, MD194, and MD211) and two metasedimentary rocks belonging to the Paleozoic (Cambrian?) Iscabambay Complex (MD112 and MD216; see Tables 1 and 2). The AFT age of MD216 was previously presented by Baby et al. (2018b) but the dataset was never published. In the SAZ, we provide the full dataset for three AFT ages of three Cretaceous to Paleogene sedimentary rocks (MD30, MD29, and MD28). These AFT ages were reported by Mora et al. (2011) and Baby et al. (2018b) but the dataset was never published. The locations of the samples are shown in Figure 3 and projected onto the cross-section in Figure 4.

The AFT analysis of the SAZ was carried out by Apatite to Zircon Inc. (former Donnelick Analytical LabAFT analyses). Sample preparation and the rest of the AFT and AHe analyses were performed at Geoscience Environment Toulouse (GET, France) and Caltech (USA), respectively, following the methodology described in Eude et al. (2015). Detailed analytical procedures can be found in the supplementary data material.

Area	Sample Name	Age	Lithology	Longitude	Latitute	Elevation (m)	ρS	Ns	ρi	Ni	ρd	Nd	P(χ²) (%)
EC	MD 170	Permo-Triassic	Plutonic rock	-7,049,500	-1,384,040	3213	231600	114	6134000	3124	1423000	41768	99,43
	MD 192	Permo-Triassic	Plutonic rock	-7,098,110	-1,359,570	3000	45540	39	1433000	1234	1367000	13741	92,44
	MD 194	Permo-Triassic	Plutonic rock	-7,091,780	-1,356,870	2385	82870	70	4796000	4283	1367000	13741	99,52
	MD 164	Permo-Triassic	Plutonic rock	-7,046,680	-1,368,790	1883	394400	186	9080000	4115	1406000	13542	81,83
	MD 211	Permo-Triassic	Plutonic rock	-7,047,750	-1,366,790	1733	180712	107	7281816	4364	1438300	14485	99,94
	MD 216	Paleozoic (Cambrian?)	Metasediment	-7,086,083	-1,334,566	986	89265	37	3508563	1403	1377758	13741	75,39
SAZ	MD 30	Late Cretaceous	Sandstone	-7,038,383	-1,318,562	382	15000	51	3085000	1051	3122000	5154	1,4
	MD 29	Late Cretaceous	Sandstone	-7,040,074	-1,314,935	371	265000	131	3787000	1875	3124000	5154	0,0
	MD 28	Miocene	Sandstone	-7,039,736	-1,312,999	366	266000	126	2413000	1142	3126000	5154	0

Area	Sample Name	Mean U (ppm)	Central Age (Ma)	Pooled age (Ma)	Mean Age (Ma)	P1 (Ma)	P2 (Ma)	Ng	TL	of Tracks	Dpar (µm)	Std (µm)	Analysts
EC	MD 170	53,9	7.9±0.8	**7.9±0.8**	8.1±1.3			28	11.03±0.5	50	2,03	1,95	ML
	MD 192	13,1	6.5±1.1	**6.5±1.1**	6.1±0.9			19	12,8	1	NO	NO	ML
	MD 194	43,9	3.4±0.4	**3.4±0.4**	3.4±0.4			26	11.15±0.6	26	2,48	1,84	ML
	MD 164	80,8	9.6±0.7	**9.6±0.7**	9.0±0.6			20	11.45±0.2	80	1,77	1,54	ML
	MD 211	63,3	5.3±0.5	**5.3±0.5**	5.4±0.3			20	11.37±0.2	103	2,17	1,8	ML
	MD 216	31,8	5.5±0.9	**5.5±0.9**	5.5±1.0			19	10.62±0.87	4	2,43	1,74	ML
SAZ	MD 30			**7.91±1.16**	13.9±3.8	**2.6±1.1 (5)**	1.6±2.0	17	13.96±0.22	21	1,84	0,99	D
	MD 29			**11.4±1.1**	11.4±1.1	**4.5±1.0 (16)**	1.9±2.1	26	13.96±0.21	53	1,69	1,51	D
	MD 28			**18.0±1.8**	13.4±3.0	**5.5±1.5 (15)**	1.6±3.5	25	13.67±0.34	18	1,8	0	D

Table 1: Fission track data. Abbreviations are as follows: EC: Eastern Cordillera; SAZ Subandean Zone; PC: Pongo de Coneq; IN: Inambari; ρs, spontaneous track density (×10^6 tracks per cm^2); N**s**, number of spontaneous tracks counted in apatite grains; ρi, induced track density in external detector (muscovite)(×106 tracks per cm2); Ni, number of induced tracks counted in micas; ρd, density of tracks on the neutron monitor; Nd, number of tracks counted in the dosimeter; Pχ2 (%), probability of obtaining χ2 value for

n degrees of freedom (where n=number of crystals - 1): if the probability is less than 5%, it is likely that the grains counted represent a mixed age population and in this case the best-fit peak age (P1-P2) were determined with BINOMFIT (Brandon 1996,2002) and are given in Ma ± 1SE; TL, mean length of measured confined tracks; ML: Mélanie Louterbach; D: Donelick; SB: Stéphanie Brichau. See supplementary material for detail in analytical procedures.

		Sample no.	Aliquot name	Mineral	n	Rs (µm)	weight (µg)	F_T	He nmol/g	U (ppm)	Th (ppm)	Sm (ppm)	eU (ppm)	Th/U	He raw age (Ma)	He corr. age (Ma)	error Abs	Std dev	Longitude (Decimal degrees)	Latitude (Decimal degrees)	Elevation (m)
EC	INAMBARI	**MD112**	A	Apatite	2	55,2	7,48	0,77	0,76	54,35	9,72	162,39	57,46	0,18	2,4	3,2	0,5		-70,8422	-13,3242	843
			B	Apatite	2	41	2,89	0,68	0,48	48,40	7,98	128,00	50,93	0,16	1,8	2,6	0,4				
		mean						**0,72**	**0,62**	**51,38**	**8,85**	**145,20**	**54,19**	**0,17**	**2,1**	**2,9**	**0,3**	**0,4**			
		MD164	A	Apatite	3	35,6	3,3	0,64	2,63	69,22	5,66	200,95	71,52	0,08	6,8	10,7	1,6		-70,4668	-13,6879	1883
			B	Apatite	3	40,4	4,33	0,71	2,52	72,12	3,47	212,23	73,94	0,05	6,3	9,0	1,3				
			C	Apatite	2	45,5	4,54	0,72	2,48	100,44	3,83	240,85	102,48	0,04	4,5	6,2	0,9				
		mean						**0,69**	**2,54**	**80,60**	**4,32**	**218,01**	**82,65**	**0,06**	**5,9**	**8,6**	**0,8**	**2,3**			
		MD169	A	Apatite	4	68,7	20,31	0,78	0,93	34,95	1035,75	472,39	288,81	29,64	0,6	0,8	0,12		-70,4865	-13,8273	2994
			B	Apatite	4	42,5	4,07	0,64	0,91	43,68	1996,70	666,90	531,95	45,71	0,3	0,5	0,08				
			C	Apatite	4	67,5	15,25	0,77	0,25	7,43	257,34	92,49	70,39	34,64	0,7	0,9	0,13				
		mean						**0,73**	**0,69**	**28,69**	**1096,60**	**410,59**	**297,05**	**36,66**	**0,5**	**0,7**	**0,06**	**0,2**			
		MD170	A	Apatite	3	34,6	2,8	0,60	1,04	57,21	356,86	328,09	145,43	6,24	1,4	2,3	0,3		-70,495	-13,8404	3213
			B	Apatite	3	34,3	2,95	0,59	1,01	46,11	264,82	283,42	111,76	5,74	1,7	2,9	0,4				
			C	Apatite	3	42,6	5,15	0,67	0,96	42,12	217,25	299,77	96,29	5,16	1,9	2,8	0,4				
		mean						**0,62**	**1,00**	**48,48**	**279,64**	**303,76**	**117,83**	**5,71**	**1,6**	**2,7**	**0,2**	**0,3**			
		MD194	A	Apatite	4	45,8	8,45	0,72	0,24	46,38	27,01	115,96	53,48	0,58	0,8	1,1	0,2		-70,9178	-13,5687	2385
			B	Apatite	3	54,8	13,53	0,76	0,15	37,91	33,19	134,75	46,60	0,88	0,6	0,8	0,1				
			C	Apatite	3	35,9	2,98	0,71	0,16	28,02	39,21	126,31	38,13	1,40	0,8	1,1	0,2				
		mean						**0,73**	**0,18**	**37,44**	**33,14**	**125,67**	**46,07**	**0,95**	**0,7**	**1,0**	**0,09**	**0,2**			
		MD211	A	Apatite	3	32,5	2,69	0,62	1,08	82,51	23,13	194,71	89,02	0,28	2,3	3,6	0,5		-70,4775	-13,6679	1733
			B	Apatite	4	36,4	4,92	0,68	0,79	79,45	30,41	260,81	88,04	0,38	1,7	2,5	0,4				
			C	Apatite	4	34,5	3,76	0,66	0,43	47,67	13,49	255,86	52,12	0,28	1,5	2,3	0,3				
		mean						**0,65**	**0,77**	**69,87**	**22,34**	**237,13**	**76,39**	**0,32**	**1,8**	**2,8**	**0,2**	**0,7**			
		MD216	A	Apatite	3	39,4	4,21	0,62	0,53	17,50	531,40	249,32	147,78	30,36	0,7	1,1	0,2		-70,86083	-13,34566	986
			C	Apatite	4	28,3	2,23	0,52	0,16	10,14	26,37	89,46	16,96	2,60	1,8	3,5	0,5				
		mean						**0,57**	**0,35**	**13,82**	**278,89**	**169,39**	**82,37**	**16,48**	**1,3**	**2,3**	**0,3**	**1,7**			

Table 2. (U-Th)/He ages were performed by laser heating for He extraction and ICP-MS for U-Th determinations at Caltech. The estimated analytical uncertainty for He ages is about 15% (2σ) due to multi-grain aliquots. Standard deviation on ages is used as error when higher than the analytical uncertainty. n = number of grains per aliquot. Multiple grain aliquots have been used due to young ages and consequently low He concentration. C*probably affected by implantation see AHe ages vs eU and Th/U

3.1.1. Thermal Modeling

To understand the significance of the results, thermal histories need to be extracted from the data. This process requires modeling software that incorporates numerical descriptions of thermal resetting in both the FT and (U-Th)/He systems. For this study, sample thermal histories were obtained using the modelling package HeFTy v2.0.9.85 of Ketcham (2005), which includes the multi-compositional AFT annealing algorithm of Ketcham et al. (2007). HeFTy software excels in reverse modeling of both AFT and AHe data. It uses a Monte Carlo approach to seek optimal cooling paths, governed by user-specified t–T boundaries. The software predicts thermal histories that align closely with the actual data collected. The modeling of each sample considers various input parameters, such as central AFT ages, track length distribution, Dpar values, and average AHe dates. When available, grain sizes and chemical attributes are also included (Table 1). The annealing multi-kinetic model of Ketcham et al. (2007) has been used for the AFT data and the radiation damage accumulation model of Gautheron et al. (2009) for the AHe data. Comprehensive results from the thermal modeling are available in the supplementary dataset.

Initial constraints used for sedimentary samples are the estimated stratigraphic deposit age (Paleogene for MD28, and Cretaceous for MD29, and 30; Louterbach, 2014) and a large box from 40°C to 200°C from the older stratigraphic age to the actual to leave maximum freedom to the software to find solutions and because of the lack of geological constraints. For the crystalline samples (MD112, 164, 169, 170, 194, 211, and 216), initial parameters were established within a temperature range of 0°C to 200°C. This range begins from an age marginally older than the previously recorded thermochronological age and concludes between 10 and 20 Ma, based on the specific thermochronological ages. This approach was chosen since the available geological data doesn't provide sufficient detail to pinpoint the thermal history prior to acquiring its AFT ages. For each sample, we tested between 10,000 and 20,000 paths. The model either continued until it found 50 suitable paths or stopped if identifying these paths proved easy for the software. Pink shading highlights the group of 50 optimal cooling paths (based on a 0.5 criterion) derived from a broader set of Monte Carlo trials (usually exceeding 1,000). The green shading indicates the range of "acceptable" paths (more than 30) within the same set, determined by a more relaxed goodness-of-fit criterion of 0.05.

3.2. Facies analyses

In the studied area Neogene deposits outcrop almost continuously along the Inambari River, from the south-western flank of the Punquiri syncline towards the Madre de Dios foredeep. Three stratigraphic sections were studied at locations I, II, and III (Figure 2). These sections were reported in Louterbach (2014, http://thesesups.ups-tlse.fr/2530/) but have never been published. The sedimentary logs corresponding to the studied stratigraphic sections have been measured at 1:500m scale during several field works between 2010 and 2012 following the methodology of Miall (1996).

3.3. Chronostratigraphy: $^{40}Ar/^{39}Ar$ step heating method

We collected a sample in a tuffaceous level dated by Gil Rodriguez (2001) at 3.23 ± 0.3 Ma (by Ar/Ar dating on biotite) and 2.96 ± 0.34 Ma (Ar/Ar dating on plagioclase). This sample (sample MD 157; longitude: -70.409 and latitude -13.1115) is stratigraphically located at ~ 2.5 km to the top of the exposed Plio-Pleistocene series between seismic horizons T3 and T4 (Louterbach, 2014). In the studied area, the tuff and enclosing layers are significantly deformed with steeply dipping beds N90E, 84 (Figure S8).

The selected sample was crushed, sieved and single grains of biotite were handpicked under binocular microscope and cleaned in an ultrasonic bath using acetone and distilled water. The minerals were packaged in aluminum foils and irradiated for 50 hours in the core of the Triga Mark II nuclear reactor of Pavia (Italia) with several aliquots of the Taylor Creek sanidine standard (28.34 ± 0.10 Ma) as flux monitor. Argon isotopic interferences on K and Ca were determined by irradiation of KF and CaF_2 pure salts from which the following correction factors were obtained: $(^{40}Ar/^{39}Ar)$ K = 0.00969 ± 0.00038, $(^{38}Ar/^{39}Ar)$ K = 0.01297 ± 0.00045, $(^{39}Ar/^{37}Ar)Ca$ = 0.0007474 ± 0.000021 and $(^{36}Ar/^{37}Ar)Ca$ = 0.000288 ± 0.000016. Argon analyses were performed at Geosciences Montpellier (France) with an analytical system that consists of: (a) an IR-CO2 laser of 100 kHz used at 5-15% during 30 sec for step-heating experiments, (b) a lenses system for beam focusing, (c) a steel sample chamber, maintained at 10-8 - 10-9 bar, with a drilled copper plate and samples on, (d) an inlet line for purification of gases including two Zr-Al getters, (e) a multi-collector mass spectrometer (Argus VI from Thermo-Fisher). Custom-made software controls the laser intensity, the timing of extraction/purification and the data acquisition. To measure the argon background within the system, one blank analysis was performed every three sample analyses. The ArArCalc software© v2.5.2 was used for data reduction and plotting. The one-sigma errors reported on plateau, isochron and total gas ages include the error on the irradiation factor J. Atmospheric ^{40}Ar was estimated using a value of the initial $^{40}Ar/^{36}Ar$ of 295.5. Results are summarized in Table S1.

3.5. Biostratigraphy

We provide two new biostratigraphic constraints from samples MD199 and MD202, collected along the Inambari River. Chunks (approximately 1 kg) of clay were collected and transported in plastic bags. For the preparation a standard procedure (dense liquid separation) of the University of Amsterdam was followed (see (Hoorn, 1993). With a knife, small blocks of approximately 1cm^3 were cut from the middle part of the clay. This sample was sieved at 212 µm. The samples were then treated with a 10% sodium pyrophosphate solution ($Na_4P_2O_7 \cdot 10H_20$). Bromoform was used to separate the inorganic/organic layers. Glycerin was used to stick the grains on the slide and paraffin was used to seal it.

Pollen and spores were counted for a maximum of two slides if the sum was less than 200, and only one slide if it contained more than 200 palynomorphs. Photographs were taken of each of the different pollen and spore types with a Optikam B5- microscope camera at a magnification of 1000x and were identified with a palynological database (Jaramillo and Rueda 2008) and several books (da Silva-Caminha et al., 2010; Germeraad et al., 1968; Hoorn, 1993; Lorente, 1986). Additional determinations were provided by Millerlandy Romero-Baez or were listed as an unknown type. The samples were dated based on the presence of biostratigraphic markers dated and using the stratigraphical zonations from Venezuela and Colombia (Jaramillo et al., 2011) . Present day family and genus associations were determined from literature (Jaramillo and Rueda, 2008).

3.6. 2-D Seismic Data

The two-dimensional seismic section Mob-97-109, acquired and processed by the Hunt Oil Exploration and Production Company of Peru and their partner Repsol Exploration Company (2009-2010), was used for stratigraphic correlation and structural interpretation in the SAZ (Figure 8). We used the software Move® to project the seismic lines, the biostratigraphic and thermochronological ages, and our field data onto the section.

3.7. Provenance analyses

3.7.1. Sr-Nd Isotopes

The Nd-Sr isotopic compositions were measured at Geosciences Environment Toulouse (GET) and were incorporated in the Master thesis of Caroline Sanchez (Sanchez, 2012). The analysed samples were first digested in hydrogen peroxide for 24 hours at ambient temperature and then digested in HNO_3 for 24 hours at 80°C followed by HF- HNO_3 for 24 hours at 80°C, and finally $HCl+HNO_3$ for 24 hours at 115°C. Blank tests were performed to estimate the level of contamination induced by the acid digestion, but it was found to be negligible. Aliquots containing about 1000 ng of Sr and Nd were loaded into the ion exchange columns. Sr and Nd were separated using the Sr-SPEC, TRU-SPEC and LN-SPEC resins (Eichrom). Nd and Sr isotopic ratios were measured using a Finnigan Mat 261 thermal ionization mass spectrometer in dynamic mode. During the Nd run, the $^{146}Nd/^{144}Nd$ (=0.7219) was used to correct the signal for mass fractionation. For each sample, checks were made for the absence of samarium (Sm). The accuracy of the measurements was estimated on the Rennes University standard for Nd (=0.511961± 14). This value was calibrated relative to the La Jolla standard by the Brest, Toulouse, and Rennes laboratories (Lacan, 2002). During the Sr run, $^{86}Sr/^{88}Sr$ (= 0.1194) was used to correct the signal for mass fractionation. The accuracy of the measurements was checked against the NBS 987 standard (=0.710240). The average values fall within the range given for these standards so that no instrumental bias needs to be considered. The repeatability on these standards is around 15 ppm. This value is adopted for the overall uncertainty of all measurements, even if some individual samples yield results with a lower internal precision. Total blanks (acid digestion plus column chemistry) for Nd and Sr were checked by ICP-MS and found to be negligible compared to the Nd and Sr amounts loaded onto the columns.

The measured $^{143}Nd/^{144}Nd$ ratios are expressed as the fractional deviation in parts per 10^4 (units) from $^{143}Nd/^{144}Nd$ in a Chondritic Uniform Reservoir (CHUR) as measured at the present day:

$$\varepsilon Nd(0) = ((^{143}Nd/^{144}Nd)S / ICHUR(0) - 1)*10^4$$

where $(^{143}Nd/^{144}Nd)_S$ is the present-day ratio measured in the sample and ICHUR(0) is the $^{143}Nd/^{144}Nd$ in the CHUR reference reservoir at the present (ICHUR(0)=0.512638 (Jacobsen and Wasserburg. 1980).

3.7.2. Detrital zircon

3.7.2.1. U-Pb geochronology

10 Neogene sandstones samples were collected on river outcrops along the Punquiri syncline. Figures S4-S7 show their stratigraphic position and Figures S9-S13 the outcrops where the samples were collected. Zircon grain separation and U-Pb analysis were conducted at the University of Brasília, Brazil. For each sample, about 7 kg of sedimentary rocks were first processed in a rock crusher, producing chips roughly 3–5 cm in size. We used a SELFRAG with a voltage of 130 kV and a frequency of 3 Hz to defragment the samples liberating the mineral phases. Heavy minerals were concentrated by panning and the magnetic fraction was removed using a FRANZ isodynamic magnetic separator. After randomly hand-picked, mounted in epoxy resin mounts and polished, back-scattered electron (BSE) images of the detrital zircon grains were obtained using a FEI QUANTA 450 Scanning Electron Microscope (SEM). The BSE images were used to identify the growth areas and zoning in zircon grains, to select suitable areas for U-Pb analysis, and to perform qualitative morphological analysis of detrital zircon grains (Figure S14). The mounts were then cleaned with 3% nitric acid before ICP-MS analysis.

About 150-200 grains were analyzed per sample with a 25μm beam using a Teledyne Iridia ablation system coupled to a Thermo Finnigan Element XR SF-ICP-MS (See Supplementary Table S3 for details). Analyses were carried out with the standard-sample bracketing method (Albarède et al., 2004). To calibrate downhole fractionation and instrument drift, zircon GJ1 (608 ± 1; Jackson et al., 2004) was used as primary reference material, and zircons 91500 (1065.4 ± 0.3 Ma; Wiedenbeck et al., 1995) and Plešovice (337 ± 0.37 Ma; Sláma et al. 2008) as secondary/validation. Data processing and correction of laser-induced fractionation (LIEF) were performed using IOLITE v4.0 (Paton et al., 2011) and VizualAge (Petrus and Kamber, 2012).

In general, measured U-Pb ages were filtered considering the quality of individual grain analysis, eliminating zircon grains with the following features: (1) high individual ^{204}Pb value; (2) high individual errors for isotopic ratios (>3%); (3)

discordances higher than 10%. For clarity, all the generated data is presented in Supplementary Table 3. Finally, the "best age" for a given zircon grain was chosen using $^{206}Pb/^{238}U$ for zircons younger than 1.5 Ga and $^{206}Pb/^{207}Pb$ ages were provided for grains older than 1.5 Ga (Spencer et al. 2016). Detrital zircon age data is visualized and compared qualitatively using kernel density estimations (KDE) diagrams and probability density plots (PDP)

To quantify the degree of dissimilarity between the detrital age distributions of the analyzed samples and investigate the contribution of recycled sedimentary units, we used the standard statistical technique called multidimensional scaling (MDS) popularized by Vermeesch (2013). The MDS method is a superset of principal component analysis that, given a table of pairwise 'dissimilarities' between samples, produces a 'map' of points on which 'similar' samples cluster closely together, and 'dissimilar' samples plot far apart (Vermeesch, 2013). Following the latest recommandations by Vermeesch (2018), we used the Kolmogorov-Smirnov test to produce an MDS map comparing the analyzed samples. The closest and second closest neighbors are linked by solid and dashed lines, respectively, and the goodness of fit was evaluated using the "stress" value of the configuration (0.2 = poor; 0.1 = fair; 0.05 = good; Vermeesch, 2013). The MDS maps were produced using the provenance package of Vermeesch et al. (2016).

3.7.2.2. Morphology

In this study, we adopted the roundness and elongation classifications proposed by Augustsson et al. (2018). This method applies solely to intact grains that display consistent U-Pb ages. For roundness, we utilized a streamlined version of Powers (1953) framework, categorizing grains as euhedral, subangular to subrounded, or rounded. As for elongation, we used the length-to-width ratios to distinguish between round (below 1.3), oval (ranging from 1.3 to 1.8), and elongated (exceeding 1.8) crystals.

4. Deformation, Exhumation, and Erosion of the Southern Peruvian EC and SAZ

4.1. Eastern Cordillera

All EC AFT ages passed the χ2 test (P(χ2)>5%) indicating that they have concordant grain age distributions (Table 1). The AFT central ages range from 3.4 ± 0.4 to 9.6 ± 0.7 Ma with MTL ranging from 10.62 ± 0.9 to 12.8 μm. AHe ages range from 0.8 ± 0.2 to 8.8 ± 2.3 Ma (Table 2). Overall, the AHe ages are younger or like their associated AFT ages. When comparing the AHe and AFT ages with elevation (Figure 5), two trends can be observed. The AFT and AHe ages increase from elevations of 986 ± 10 to 1883 ± 15 meters above sea level (m.a.s.l.). Our AHe ages are like those of Lease and Ehlers (2013) collected at the same elevation (e.g., MD211 sampled at ~1733 m.a.s.l. and 11PR04 sampled at ~1759 m.a.s.l., Figure 5, Table 2). Above ~1900 m.a.s.l. a marked shift toward younger AHe and AFT ages is observed. The lowest samples and those which are in the footwall of the Ollachea fault (MD 211 and MD164, Figures 2 and 4) have older AHe and AFT ages than the samples located in the hanging wall of the fault (MD 194 and MD169). The thermochronological ages might indicate a large Plio-Pleistocene uplift of the Ollachea hanging wall (Figures 4 and 5). Additionally, the thermal histories derived from the inverse modeling of thermochronometer ages using the HeFTY software (Figure 6) further indicate rapid Plio-Pleistocene cooling between 1 and 3 Ma while before the samples may have stayed in the Partial Annealing/Retention Zone during an extended period (probably at least 4-5 Ma,).

3.1.3. Sub-Andean Zone

The Punquiri syncline may show a late Miocene-Pleistocene growth strata. These growth strata are highlighted by dip data projected onto seismic line Mob-97-109 (Figure 7). The growth strata from the Punquiri syncline can thus be correlated with those that are located above the late Miocene marker T2 registered in the Pongo de Coñeq area and are interpreted to be mostly late Miocene to Pliocene in age (Louterbach, 2014). Pliocene deformation is further attested by the presence of significantly deformed tuff and enclosing layers with steeply dipping beds (N90, 84E). This tuffaceous level, situated between seismic horizons T3 and T4 was dated to 3.45±0.15 Ma using the Ar-Ar method.

In the SAZ, the three sandstones (MD28, MD29, and MD30) dated with the AFT method failed the $\chi 2$ test with $P(\chi 2)$ being less than 1.4% (Table 1; Figure 6b). The best-fit peaks in each fission track grain age distribution were determined based on a binomial model described by Galbraith (1988) and Galbraith and Green (1990) using the BINOMFIT program (Brandon, 1992, 1996, 2002; Figure S2). The youngest peak ages for samples MD28, MD29, and MD30 are 5.5 ± 1.5 Ma, 4.5 ± 1 Ma, and 2.6 ± 1.1 Ma, respectively (Table 1). The youngest peak age is the dominant component for samples MD28 and MD29 containing 60% and 64% of the distribution, respectively. The youngest peak age of sample MD30, although not dominant, represents a significant part of the grain ages (~30%). The HeFTy of these samples suggests that the AFT ages are reset AFT ages (Figure 8).

4. Late Miocene-Pleistocene depositional evolution in the Madre de Dios Basin

In summary, the approximately 3300m thick late Miocene-Pleistocene deposits can be divided into lower and upper intervals. The lower ~2000 m are interpreted as sand-dominated deposits. The upper ~1300 m are characterized by an abrupt change to conglomerate-dominated deposits. The two sections are separated by erosive unconformities or by a stratigraphic gap. The full composite stratigraphic section can be found in detail in the Supplementary Dataset (Figures S4-S7) and is summarized in Figure 9. The sedimentary facies and facies association for these deposits are found in Tables 3 and 4, respectively.

We also report two new biostratigraphic ages and one $^{40}Ar/^{39}Ar$ age on biotite from a tuffaceous level in the Punquiri syncline (MD204). Samples MD199 and MD202 were dated based on their palynological content. The presence of *Echitricolporites spinosus* (17.41-0.14 Ma, Jaramillo et al., 2011), *Proteacidites triangulates* (24.13-3.41 Ma, Jaramillo et al., 2011) and *Cyatheacidites annulatus* (7.15-0.11 Ma, after Jaramillo et al., 2011) in the MD199 and MD202 samples suggest a late Miocene to Pliocene (ranging between 7.15 and 3.41 Ma) depositional age (Table S1; Figure S8). Our new radiometric age documented for outcrop MD 157 (3.45±0.15 Ma; Table S2; Figure S9) is consistent with the radiometric age obtained by Gil Rodriguez et al. (2001) in the same area (3.23±0.3 Ma).

Facies Code	Lithofacies	Sedimentary structures/other characteristics	Interpretation
Gh	Clast-supported conglomerates. Granule to boulder, subrounded to well-rounded	Trough cross-stratification, normal grading with imbrications	Transverse bar, minor channel fill
Gm-Gmf	“Mud-breccias”. Matrix-supported to clast-supported conglomerates (Gravel to pebble)	Planar cross-stratification	Linguoid bar, transverse bar
Sr	Sandstones. Very fine to medium-grained, occasionally pebbly. Moderate sorting	Rippled cross-stratification (climbing ripples)	2D or 3D ripples, upper flow regime
Sp	Sandstones. Very fine to medium-grained, occasionally pebbly. Moderate sorting	Planar cross-bedded, possible mud clasts at the base	Linguoid, transverse bar
Sh	Siltstones or very fine- to coarse-grained sandstones	Horizontal lamination	Planar bed flow (lower or upper flow regime)
St	Very fine- to coarse-grained sandstones	Trough cross-stratification	3D dune migration
Stmc	Very fine- to very coarse-grained sandstones, with scattered to aligned pebbles	Trough cross-stratification, highlighted by mud clasts or occasional lithoclasts (mm to pluri-cm). Occasional wood fragments.	Seasonal regime. 3D dune migration
Sm	Massive sandstones (fine to coarse-grained, with possible scattered to aligned pebbles) moderate to well sorted	No structure. Occasional wood fragments	Rapid deposition, gravity flow
Sfu	Massive sandstones (fine to very coarse-grained), finning upward	Frequently aligned mudclasts and lithoclasts at the base. Occasional wood fragments.	Fluvial bedforms and bars, waning flood
Scu	Massive sandstones (fine to very coarse-grained), coarsening upward	Frequently aligned mudclasts and lithoclasts at the base. Occasional wood fragments	Crevasse splay
Sb	Very fine- to medium-grained sandstones (reddish-yellow)	Bioturbation (continental)	
Fl	Siltstones, mudstones	Lamination, very small ripples. Occasional flame-structure. Occasionally calcareous	Overbank or waning flood deposits

Fm	Siltstones, mudstones	Structureless. Occasionally calcareous	Overbank or waning flood deposits
Fb	Mudstones to siltstones (red to purple)	Bioturbated (continental). Red to green.	Overbank or abandoned channel, incipient soil
Fbl	Mudstones to siltstones (blue to grey/dark grey)	Structureless or some ripples	Backswamp, oxbow-lake, anoxic environment
P	Mudstones to siltstones (red to purple). Carbonaceous nodular, gypsum levels	Frequent bioturbation and rootlets, carbonaceous nodules, and stratified gypsum. Possible ferruginous pisoliths	Paleosoil
T	Tuffaceous deposit. May be micaceous	Structureless, rippled, or with planar lamination. Some wood debrites	Volcanoclastic lacustrine deposits

Table 3. Summary of the Neogene lithofacies and interpreted depositional environments in the Madre de Dios retroarc foreland basin (modified from Miall, 1996)

	Interpretation	Facies
FCcg	Braided (?) river. Mainly gravelly to conglomeratic fluvial channel filling	Gh, Gp, Gt, Stmc, St, Sm, Sh, Sfu
FCs	Meandering fluvial channel filling with conglomeratic levels at the base	Sfu, Sm, Sr, Sh, Sp, St, Stmc, Fl, Gt, Gh, Gp, Gm-Gmf, (Fb)
O	Overbank: abandoned channel, waning flow deposit and paleosol, continental swamp or oxbow lake (Osw). Possible coarsening upward sandy crevasse splays (Ocp)	Fm, Fl, Fb, P, Sfu, Sm, Scu, Sr, T

Table 4. Facies association for the Neogene deposits in the Madre de Dios retroarc foreland basin

4.1. Lower section: sandstone-dominated interval

4.1.1. Fluvial channel sandy deposits (FCs)

Description: Facies association FCs is mainly made up of arkosic fine- to coarse-grained sandstones fining upsection into fine-grained to silty deposits (Figure 9). Sandy to gravelly conglomeratic facies may be occasionally present at the base of the fining-upward units. The base of facies association FCs is characterized by a slight deeply erosive and channelized surface. A 10 to 30-cm-thick mud breccia (Gm, Table 1) can also occur at the base of the facies association. Clasts (<2 cm) are angular to subrounded and consist of reworked mud clasts and extraformational ferruginous clasts (Gmf, e.g., in Section 1, at 1175 m, Figure S4). These Gm deposits can be either clast- or matrix-supported. The basal parts of the channel infillings can also be constituted by Gt, Gh, or Gp facies (Table3). Gt facies corresponds to conglomeratic deposits, 30 cm- to more than 3 m-thick, with trough crossbedding. Gh and Gp facies correspond to horizontally and planar bedded conglomerates, respectively, with normal to inverse grading and occasional pebble imbrications. The channel fillings typically evolve upsection into fine- to medium-grained sandstones. These sandstones are 10 cm to pluri-metric thick and can be massive (Sm), with trough cross-stratification (St), with planar (Sp), or horizontal bedding (Sh). Frequent mud clasts commonly highlight the sedimentary structures, particularly the trough cross-bedding structures situated at the base of the sandy channel-shaped bodies (Stmc). The top of Facies association FCs is characterized by 10 cm-100 cm thick finer deposits such as fine-grained rippled sandstones (Sr) or laminated siltstones to mudstone (Fl). Facies Sfu corresponds to 50-300 cm-thick fining-upward sandstones. Overall, facies association FCs corresponds to a single thick channelized sedimentary unit ranging in thickness between 50cm and 5m, or a series of 1m to 30m sandy stacked channel filling units (vertically stacked CH components). There are no lateral accretion characteristics.

Interpretation: The channel-shape geometries and fining-upward sequences show that facies association FCs is mostly generated by sandy stream floods at the end of significant flow episodes in the channels. The repeated vertical stacking patterns of the fining-upward units suggest that flow velocity fluctuates regularly. The presence of facies Sp, St, and Sh (Figure 10), as well as the lack of lateral accretion features, imply that sand bodies are the result of limited, high-energy stream floods and record deposition linked with subaqueous dunes and upper-stage flat beds (Miall, 1996).

Facies Sm corresponds to massive sandstones deposited during sediment gravity flow or rapid deposition. Facies Sfu, Sr, and Fl, situated at the top of the channel filling sequences, are associated with a loss of stream flood energy during the channel abandonment phase. The poorly developed, disorganized, and matrix-supported conglomeratic bedforms (Gm-Gmf) described at the base of the sequences suggest high sedimentation fallout rates and/or shallow flow depth (e.g., in Jo et al., 1997; Uba et al., 2005). We interpret facies Gt, Gh, and Gp as being deposited by occasional high energy stream floods equivalent to those produced by gravel-laden streams in poorly to well-confined channels (e.g., in Ridgway and DeCelles, 1993; Uba et al., 2005). Because facies association FCs is associated with continental fine-grained overbank deposits (O) the sandy facies of FCs have been interpreted as fluvial channel-filling deposits. Depending on the geometry of the sandy units and their vertical stacking pattern, deposits can be associated with a single-story fluvial channel (single fining-up sandy unit) or multi-stories channel complex (sandy units displaying an important vertical stacking).

4.1.2. Overbank deposits (O)

<u>Description:</u> Facies association O is common in the studied sedimentary sections (Supplementary Figures S4-S7) and frequently overly the FCs and FCg associations. It consists of massive mudstone or siltstone (facies Fm, Table 3), laminated mud or silt deposits (facies Fl, Table 3), bioturbated reddish or varicolored mudstone to siltstone (facies Fb, Table 3) or blue to dark structureless or rippled mudstone to siltstone (Facies Fbl, Table 3) occasionally interbedded with silty or sandy bodies. Facies Fb can also present occasional desiccation traces. In muddy Root traces, carbonates nodules, and bioturbations can often be observed in muddy to silty layers these fine-grained overbank deposits range from 20 cm- to 20 m in thickness. Coarser-grained sandy deposits with thicknesses ranging from 20 to 200 cm of massive or fining-upwards fine-grained to medium-grained sandstones (Sm or Sfu), rippling sandstones (Sr), or coarsening-upwards sandstone (Scu) can be intercalated within the fine-grained overbank deposits. Additionally, within the overbank fine-grained sequences of the Inambari transect, two tuffaceous layers have been described (outcrop MD 2019-08 at 1615 m in Figure S2 and outcrop MD 2019-09 at 2465 m in Figure S5). These tuffaceous layers range in thickness from 30 to 100 cm and may exhibit ripples or flat

horizontal sedimentary features (T, Figure 11-C). These facies are rich in wood pieces and leaf remnants.

Interpretation: Palynomorphs determined in MD 199 and MD 202 suggest a continental paleoenvironment for this facies association (Table S1). Furthermore, the facies of facies association O are usually strongly associated with facies associations FCs and FCcg, both of which are interpreted as continental. We interpreted that facies association O represents deposition in a floodplain environment (Fm, Fb, Fbl, P) occasionally disturbed by waning flow deposits (Sr, Sm, Fl) and crevasse sand bodies (Scu). Facies Fm represents deposition from low-energy flows or from standing water pools after channel abandonment (Miall, 1996). The absence of desiccation cracks, the existence of sporadic root traces, and the general reddish-to-purple color of Facies Fb imply oxidizing circumstances (e.g., Turner, 1980; Miall, 1996; Retallack, 1997) with common subaerial exposure (e.g., Esteban and Klappa, 1983). The dark color of facies Fbl and its proximity to a fluvial system are consistent with deposition in an anoxic environment such as an oxbow lake or continental swamp (Miall, 1996). The thin carbonate layers, occasional carbonate nodules, and numerous root traces and continental bioturbation of facies P show pedogenic alteration following deposition (e.g., Wright and Tucker, 1991; Retallack, 1997) and are linked with a well-developed paleosol horizon. Thin layers of fine-grained silty to sandy deposits organized by thin lamination and occasional ripples (Fl and Sr) might be suggestive of low-energy streams (waning floods) linked with deposition in remote floodplains (e.g., Uba et al., 2006). The sporadic coarsening-upward and massive sandstones of facies Sm and Scu can be attributed to crevasse splay deposits and crevasse-channel fills that occur in a proximate floodplain environment. It should be noted that these sandy units can be found in some sedimentary successions regarded as overbank deposits and may represent evidence of active channel avulsion processes at the time (e.g., DeCelles and Horton, 2003).

4.2. Upper Interval: conglomerate-dominated deposits

4.2.1. Fluvial channel conglomerate deposits (FCcg)

Description: Facies association FCcg occurred mostly in the Plio-Pleistocene deposits although it can be present in the Miocene sedimentary rocks (Figure S6). It is associated with facies associations O (overbank) and FCs (Fluvial channel sandy deposits). Its thickness ranges between 2 and 15 m. Facies association FCcg always starts with an erosive surface overlaid by the conglomerate deposits with trough cross-bedding (Gt, see Table 1 for detailed facies descriptions) and planar or horizontal bedding (Gp and Gh, respectively). The matrix of the clast-supported conglomerate facies consists of medium to very coarse-grained arkosic sandstone. Conglomerate bodies are 1m to 3 m thick. They can evolve upwards into finer-grained deposits, displaying an overall fining-up trend, or be eroded by another conglomerate body forming then an important stacking pattern (see Figures S5 and S6, from 2309 to 2407m). Clasts are dominated by metamorphic and granitic, can be up to > 40 cm in diameter, are sub-rounded to well-rounded, and are moderately sorted. The clast-size distribution is polymodal and shows inverse to normal grading. Imbricated clasts are present. Finer-grained deposits of facies association FCcg can be massive or fine upward from very coarse to fine-grained sandstones (Sm, Figure 11-D and Sfu, respectively), sandstones with trough cross-bedding (St, Figure 11-E) occasionally highlighted by mud clasts (Stmc), and sandstones with planar bedding (Sp). Outcrop MD 206 shows this fining-up trend from conglomerates to sandstone facies (Figure S6, from 2805 to 2825 m).

Interpretation: Occasional cross-stratification and rare clast imbrications of the clast-supported pebble-to-boulder conglomerates facies associated with basal erosive surfaces suggest deposition from high-energy floods such as those produced by gravel-laden streams in poorly to well-confined channels (e.g., in Ridgway and DeCelles, 1993; Uba et al., 2005). The organized clast-supported conglomerate facies (Gt, Gh, and Gp) with weak imbrications may be the result of incised-channel gravel bedload sedimentation under low- to waning-energy flows (Jo et al., 1997; Uba et al., 2005). This interpretation is supported by the presence of frequent erosive surfaces associated with overall stacking patterns. Consequently, Gt, Gh, and Gp facies may correspond to transverse or lingoid bars (Miall, 1996). Trough cross-bedded sand (St) and conglomerate bodies (Gt) mainly represent channel deposits (Miall, 1996). Sandy facies such as Sfu, Sm, Sp, or Sh deposits are less frequent and mainly situated at the top of the fining-up sequences. They are interpreted to have been deposited following a loss of energy from the stream floods. Because facies association FCcg is strongly associated with the Overbank facies association (O), where only continental palynomorphs have been found (Table S1), it is interpreted to be deposited by high-energy braided fluvial rivers deposits laterally changing into a fine-grained fluvial floodplain environment.

4.3. Provenance

4.3.1. Sr-Nd Isotopes

The $^{87}Sr/^{86}Sr$ isotopic composition of five fine-grained Neogene samples analyzed ranges from 0.72475 to 0.73358, and the ƐNd is between -11.7 and -12.6 (Table 5). The Sr-Nd isotopic fingerprint of suspended particulate matter (SPM; Allègre et al., 1996; Viers et al., 2008; Santos et al., 2015; Rousseau et al; 2019) and bulk mudstone (Roddaz et al., 2005b; Hoorn et al., 2017; van Soelen et al., 2017; Hurtado et al., 2018; Chavez et al., 2022; Moizinho et al., 2022) has been extensively used as provenance tracer to distinguish between Andean and cratonic sources in different Amazonian rivers. In Figure 12 we plotted the $^{87}Sr/^{86}Sr$ and ƐNd(0) composition of relevant Andean sources and the SPM from the main tributaries in the Amazon drainage basin. Our data highlights that all analyzed Neogene mudstone samples from the Madre de Dios Basin fall into the Sub Andean Zone isotopic fingerprint. This is the same field of the present-day SPM transported by the Madeira River, and of other sedimentary rocks from the south Amazonian foreland basin (SAFB; Roddaz et al., 2005b).

Sample	Age	Sr (ppm)	Nd (ppm)	$^{87}Sr/^{86}Sr$	±2σ	$^{143}Nd/^{144}Nd$	±2σ	ƐNd(0)
MD197	Early Miocene	113,2	51,37	0,724753	9	0,512038	6	-11,7
MD199	Late Miocene-Pliocene	102,4	44,17	0,733581	7	0,511991	5	-12,6
MD 200B	Late Miocene-Pliocene	117,9	41,65	0,728020	11	0,511997	5	-12,5
MD 202D	Late Miocene-Pliocene	86,33	38,49	0,728579	8	0,512011	6	-12,2

MD 204B	Pliocene	106	40,16	0,729826	12	0,512023	7	-12

Table 5. Sr-Nd isotopic compositions of the analyzed Neogene sedimentary rocks from the Madre de Dios foreland basin.

4.3.2. Detrital zircon U-Pb ages and morphology

Of the ten samples examined, three originate from the lower sand-dominated interval, while the remaining seven hail from the upper conglomerate-dominated interval (refer to Figure 9). Results of the U-Pb isotope analyses are detailed in Table S3 and showcased in Figure 13. Predominantly, the principal zircon age groups fall between 900-1300 Ma (Grenville/Sunsás) and 500-700 Ma (Brasiliano/Pampean), together making up an average of 53% of all grains studied. Another discernible group, spanning 250-130 Ma (Triassic-Jurassic), appears in every sample and constitutes an average of 15.2% of the grains. Additionally, less dominant populations from both the Precambrian and Phanerozoic eras are evident, particularly within the 1300-1540 Ma (Rondonia-San Ignácio), 500-400 Ma (Famatinian), and 400-250 Ma (Paleozoic) clusters. While these age groups are consistently present across the section, a minor fluctuation in the proportion of Triassic ages can be noticed from sample MD2019-5A to MD2019-16B. It seems that during periods of increased Triassic on the detrital zircon population, there was a corresponding decrease from other age groups.

Zircon grains generated during the Grenville/Sunsás and Brasiliano/Pampean orogenies can be found elsewhere in the Coastal Cordillera, Altiplano, Eastern Cordillera, or Amazonian Craton, and thus are not useful to discriminate between Andean and cratonic sources (Chavez et al., 2022). The presence of zircon grains younger than 500 Ma in all analyzed samples typifies an Andean provenance (Chavez et al., 2022 and references therein). Famatinian (500-400 Ma) rocks occur in isolated Ordovician intrusions of the Marañon and Arequipa massifs (Ramos, 2009; Loewy et al., 2004). Perez and Horton (2015) also reported Famatinian detrital zircon populations in the Oligocene-Miocene sedimentary rocks from the Ayaviri Basin, a hinterland basin in the northern Altiplano Plateau, approximately 200 km southwest of the studied area. Permo-Triassic (290-216 Ma) magmatism was active along the entire length of the Peruvian Eastern Cordillera (Kontak et al., 1985; Clark et al., 1990; Soler and Bonhomme, 1990; Sempere et al., 2002; Miskovic et al., 2009; Boekhout et al., 2018). Several Permo-Triassic plutons have been mapped in the southwest portion of the studied area (Figure 3). Middle to Late Triassic (245-220 Ma) ages are recorded by the volcano-sedimentary rocks of the Mitu Formation (Spikings et al. 2016) and batholiths (Sempere et al., 2002) in the Cordillera de Carabaya region. Jurassic (201-145 Ma) rocks in the Central Andes are associated with the Jurassic magmatic arc and attributed to extensional processes across the western Gondwana margin (Oliveros et al., 2012; Boekhout et al., 2013). Finally, zircon grains younger than 130 Ma, are characterized as the Andean arc (Chocolate and Toquepala arcs) and typify a Coastal Cordillera provenance (Chavez et al., 2022).

We compared our dataset with Paleozoic metasedimentary rocks from the Eastern Cordillera (Reimann et al., 2010; Bahlburg et al., 2011), the Middle to Late Triassic Mitu Group (Perez and Horton, 2015; Spikings et al., 2016), the Cretaceous Huancané Formation (Spikings et al., 2016) and the Paleocene sedimentary rocks from the Madre de Dios Formation (Louterbach et al., 2018b). In the MDS map (Figure 14A) the upper Miocene-Pliocene samples plot scattered, and no cluster can be discriminated, even between samples of similar depositional ages. However, our samples plot right in between the compiled detrital zircon ages dataset. This configuration might indicate a continuous input of recycled sediments in the Madre de Dios Basin and that although the proportion of the contribution of each source might oscillate over the Late Miocene-Pliocene, the sources were kept the same. On the other hand, even though connected by a solid line with one of the Neogene samples (MD2019-14A), the overall high dissimilarity with the Mitu Group might suggest that the reworking of this unit was either discrete or unlikely.

Zircon morphological analyses were performed on unbroken grains with concordant ages. The results are summarized in Table S3 and illustrated in Figures 15 and 16. Overall, the zircon grains exhibited a diverse range of lengths, spanning from 73 µm to 228 µm, and most were categorized as rounded and elongated. There seems to be a noticeable trend of a rise in the percentage of euhedral grains between samples MD2019-09B and MD2019-14A, which might indicate an increase on first cycle sediments (Augustsson et al. 2018). Furthermore, we explored the correlation between zircon grain shape, U-Pb ages, and potential zircon-producing events (Figure 16a). In our dataset, the prevalent zircon populations - Grenville, Brasiliano, and Triassic – are consistently present in both oval and elongated shapes forms across samples. Notably, zircons with elongation exceeding 3 are more prevalent in the Triassic populations than in the Brasiliano and Grenville (Figure 16b).

5.Discussion

5.1. Neogene deformation of the Sub-Andean Zone

The Oligocene-middle Miocene period of thrust deformation has been recorded in the EC and Altiplano zones adjacent to the study area (Perez and Horton, 2014; Horton 2018). Growth strata recorded along the footwall of the Ayaviri thrust fault indicate that thrust deformation along the southwest-directed, northeastern basin margin of the Ayaviri thrust fault, was active at around 28-26 Ma at the EC/Altiplano boundary (Perez and Horton, 2014). Additionally, an abrupt middle Miocene shift to coarse alluvial fan deposition sourced from the Western Cordillera is interpreted to have been driven by out-of-sequence deformation along the northeast-directed, southwestern basin margin of the Pasani thrust at 18–16 Ma (Perez and Horton, 2014). This northern Altiplano out-of-sequence deformation was coincident with the structurally driven exhumation of the EC at 15-16 Ma as recorded by the He dates of zircon grains from the Coasa pluton and Rio San Gabán transect located in the EC (Perez et al., 2016). Paleo elevation models based on hydrogen isotopic compositions of hydrated volcanic glasses and modern stream waters suggest that the EC was slowly elevated 1.5–2 km between 25 and 10 Ma, which rate is interpreted to be consistent with crustal shortening as the dominant driver of surface uplift (Sundell et al., 2019). In our study area, there is no thermochronological or sedimentary record of deformation before the late Miocene.

5.2. Late Miocene-Pliocene

Overall, our dataset suggests that the southern Peruvian EC and SAZ have been deforming, uplifting, and propagating forward since the late Miocene as evidenced by late Miocene to Pliocene AFT and AHe ages related to out-of-sequence thrusting in the EC; and by the presence of growth strata geometry in the SAZ (Punquiri syncline) in response to the duplex formation and development of piggyback synclines

(Figure. 15). Similar piggyback basins associated with duplexes in the hinterland have been documented in the Bolivian and Peruvian SAZ (Baby et al., 1995; Espurt et al., 2011; Mora et al., 2014; Parra et al., 2010). Analog modeling of the Bolivian SAZ suggests that the dominance of sedimentation over erosion in the foreland basin favors the forward propagation of the frontal thrust and development of piggy-back basins (active depositional basins between thrust structures; Leturmy et al., 2000). Mora et al (2014) proposed that a period of late Miocene topographic growth and an associated increase in accommodation and sedimentation rates favor the development of duplexes in the Inambari area of the southern Peruvian SAZ. Our data agree with these findings, especially regarding the Plio-Pleistocene units, in which syntectonic growth strata are associated with the development of duplexes, piggy-back synclines, and the forward propagation of the SAZ and input of recycled sedimentary rocks of the SAZ to the late Miocene-Pleistocene piggy-back syncline sediments.

Our provenance proxies show that the source of sediments being eroded in the southern portion of the Madre de Dios basin did not change significantly throughout the Neogene (Figure 13). Besides the always present Precambrian ages from the crystalline basement found elsewhere in the Andes and Western Amazonia, the Permian, Triassic, and Jurassic were the main detrital zircon ages populations observed. These ages represent different extensional magmatic events, and their distribution varies across strike in the Eastern Cordillera (Chavez et al., 2022). In fact, our data reveals a high similarity between the detrital zircon populations and Sr-Nd isotopic compositions of Late Miocene -Pliocene sedimentary rocks and older SAZ sedimentary successions which supports the input of recycled Paleozoic to Cretaceous sediments from the SAZ (Figures 14 and 15). This hypothesis is further supported by the rounded nature of most grains observed, signaling longer transportation processes or sediment recycling.

However, the observed increase on the proportion of Triassic-aged zircons, together with the reduced presence of Grenville and Brasiliano zircons and an increase in euhedral grains between samples from the upper interval (MD2019-09B to 16B), might indicate that, for a time, a Triassic terrain was more fertile and sourced the Madre de Dios basin with first cycle zircon grains. Permo-Triassic plutonic rocks crop out extensively on the EC (see Figure 3a), which we interpret to suggest erosion of the EC.

These results are consistent with what is recorded in the central Peruvian SAZ, north of our study area, where the Pliocene reactivation of Paleozoic thrusts has also been observed (Gautheron et al., 2013). In that region, 23 km of shortening affecting the Camisea SAZ (12°S) has accumulated since 6 Ma (Espurt et al., 2011), demonstrating that a significant amount of deformation has affected the EC-SAZ since the Pliocene. This is also consistent with the Ecuadorian, Bolivian and Argentinian Andes where the Sub-Andean thrust wedge has continued propagating until the present and notably during the Plio-Pleistocene (Horton and DeCelles, 1997; Echavarria et al., 2003; Uba et al., 2009a; Espurt et al., 2011; Gautheron et al., 2013; Eude et al., 2015; Anderson et al., 2018; Margirier et al., 2022). Additionally, the propagation of the Sub-Andean thrust wedge could also be supported by the overall coarsening-up trend of the Madre de Dios SAZ's Neogene sedimentary infill, which we interpret as a depositional megasequence characterized by a significant rise in sedimentation rates. This is demonstrated by the presence of distal sand-dominated deposits in the Neogene (lower interval), which evolved into conglomerate-dominated deposits in the Late Miocene to Pleistocene (upper interval) periods (Figures 9 and 15).

5.3. Tectonic vs. Climatic controls in the erosion of the EC and SAZ

Large scale kinematics of fold and thrust belts obey the theory of a tapered orogenic wedge (Chapple, 1978; Davis et al., 1983; Dahlen, 1984, 1990; Dahlen et al., 1984; DeCelles and Mitra, 1995). This suggests that the fronts of orogenic wedges develop taper toward their undeformed forelands and advance when the sum (θ) of their basal (β) and upper (α) slopes reach a critical value θc. When changes in (β) and (α) force the wedge out of the critical state into a "supercritical" or "subcritical" state, the wedge responds by deforming to alter its geometry until the critical condition is regained (DeCelles and Mitra, 1995; Horton, 1999). For instance, an orogenic wedge that becomes subcritical may attempt to regain a critical state through internal deformation by out-of-sequence thrusting, synchronous thrusting, or duplexing (e.g., Boyer, 1992; DeCelles and Mitra, 1995; Mitra and Sussman, 1997; Horton, 1999; Uba et al., 2009b). In turn, processes such as erosion, which reduce surface slope, may ultimately tend to induce internal deformation within the wedge (DeCelles, 1994; DeCelles and Mitra, 1995). We interpret the surface uplift of the EC, as the presence of out of sequence thrusting and the EC provenance of Neogene sedimentary rock as indicating that the southern Peruvian Amazonian EC and SAZ orogenic wedge existed under subcritical conditions. This is consistent with previous studies suggesting that the propagation and width of the Andean orogenic wedge has been limited by focused erosion (Horton, 1999) on the EC, potentially driven by a wetter climate since the Miocene (McQuarrie et al., 2008b).

Many studies have emphasized the potential climatic controls on the Neogene erosion, exhumation, and deformation in the EC and SAZ (McQuarrie et al., 2008b; Uba et al., 2009b; Lease and Ehlers, 2013). In the studied area, Plio-Pleistocene climatic forcing has previously been inferred based on the presence of widespread Pliocene AHe erosional cooling ages in the EC and from the assumption that tectonic activity has been lacking for the past 4 My both in the EC and SAZ (Lease and Elhers, 2013). This Pliocene erosion of the Bolivian and southern Peruvian EC has been interpreted as being controlled by a “shift in global climate from early Pliocene warmth to late Pliocene cooling driven by sea surface temperature changes”. It is possible that after having reached a critical elevation in the Miocene leading to higher rainfall and erosion gradients across the EC, focused erosion led to accelerated exhumation and increasing deformation in the adjacent SAZ. Such a climatic forcing has been invoked in the EC of Colombia to explain the differences in exhumation and deformation rates between a drier western flank and a humid eastern flank (Mora et al., 2008) although this view has recently been challenged (Pérez-Consuegra et al., 2021). Our thermochronological cooling ages advocate for Plio-Pleistocene uplift and related erosion both in the EC and the SAZ, consistent with the ~ 4 Ma cooling age data presented by Lease and Ehlers (2013). In contrast with the climatic driver of exhumation proposed by these authors, coeval uplift induced the exhumation of the SAZ, the EC, and Pliocene growth strata, which all support the 4 Ma to present tectonic uplift in the EC as an important driver of exhumation; these also provide evidence against the assumption that deformation was absent in the SAZ during this time.

6. Conclusions

The combination of fieldwork, structural and stratigraphic sections interpretation of depositional environments, AFT and AHe ages, interpretations of a new subsurface dataset, and provenance data from the Eastern Cordillera and Sub Andean Zone show that significant deformation occurred in the Amazonian orogenic wedge of southern Peru during the Late Miocene-Pliocene, even though climatic changes may have enhanced erosion or modified erosional processes. The late Miocene to Pliocene deformation is recorded by AFT and AHe ages in both the EC and SAZ and by growth strata geometry in the SAZ. This period is characterized by 1) the development of piggy-back synclines and duplexes in the SAZ, as well as the overthrusting of the EC and input of recycled sedimentary rocks of the SAZ to the late Miocene-Pleistocene piggy-back syncline sediments. Additionally, the transition from distal low energy fluvial system in the Early Miocene (lower section), to a high energy proximal fluvial system in the Late Miocene to Pleistocene (upper section) indicates an increase in sedimentation rates, thus our data show that the thrust wedge has continued propagating until the present, following a period of notably active propagation during the Plio-Pleistocene.

Acknowledgments

This work received financial and institutional support from Repsol S.A., Perupetro, and the IRD (Institut pour la Recherche et le Développement). Patrick Monié is thanked for his help and interpretation of Ar dating results. We thank Jean-Claude Soula, Patrice Baby, and Stéphane Brusset for their helpful comments and discussions on previous drafts of this paper. This paper is also dedicated to the memory of Jean-Claude Soula who passed away in 2020. This work was part of the Ph.D. project of Melanie Louterbach which has been sponsored by Repsol. This study was also supported and funded by CAPES-COFECUB program Te 924/18/ 88881.143095/2017–01 “Paléo-Amazone: evolution Néogène de l’Amazonie Brésilienne/O PALEO AMAZONAS: evolução neogênica da Amazônia Brasileira”” and by the joint Brazilian-European facility for climate and geodynamic research on the Amazon River Basin sediment (CLIM-AMAZON) project. We thank German Bayona and Mauricio Parra as well as the editor Andres Folguera for valuable reviews that improved this contribution.

References

Albarède, F., Telouk, P., Blicheret-Toft, J., Boyet, M., Agranier, A., Nelson, B. 2004. Precise and accurate isotopic measurements using multiple-collector ICPS. *Geoch. et Cosm. Act.* 68(12), 2725-2744.

Allègre, C.J., Dupré, B., Négrel, P., Gaillardet, J., 1996. Sr-Nd-Pb isotope systematics in Amazon and Congo River systems: constraints about erosion processes. Chem. Geol. 131, 93–112. https://doi.org/10.1016/0009-2541(96)00028-9.

Anderson, R. B., Long, S. P., Horton, B. K., Thomson, S. N., Calle, A. Z., Stockli, D. F. 2018. Orogenic Wedge Evolution of the Central Andes, Bolivia (21°S): Implications for Cordilleran Cyclicity. *Tectonics* 37, 3577–3609. doi: 10.1029/2018TC005132.

Antoine, P.-O., Roddaz, M., Brichau, S., Tejada-Lara, J., Salas-Gismondi, R., Altamirano, A. 2013. Middle Miocene vertebrates from the Amazonian Madre de Dios Subandean Zone, Perú. *J. South Am. Earth Sci.* 42, 91–102. doi: 10.1016/j.jsames.2012.07.008.

Augustsson, C., Voigt, T., Bernhart, K., Kreißler, M., Gaupp, R., Gärtner, A., Hofmann, M., and Linnemann, U., 2018, Zircon size-age sorting and source-area effect: The German Triassic Buntsandstein Group: Sedimentary Geology, v. 375, p. 218–231, doi:161 10.1016/j.sedgeo.2017.11.004.

Apatite to Zircon Inc., 2004. Peru samples: Apatite and Zircon Fission-Tracks data.

Baby, P., Calderon, Y., Hurtado, C., and Bandach, A. 2018a. *Atlas of the Peruvian Subandean Petroleum Systems From source to trap*. Perupetro and IRD. Lima Available at: https://www.researchgate.net/publication/334042013_ATLAS_OF_THE_PERUVIAN_SUBANDEAN_PETROLEUM_SYSTEMS_-_From_source_to_trap.

Baby, P., Calderón, Y., Hurtado, C., Louterbach, M., Espurt, N., Brusset, S., et al. (2018b). "The Peruvian Sub-Andean Foreland Basin System: Structural Overview, Geochronologic Constraints, and Unexplored Plays," in *Petroleum Basins and Hydrocarbon Potential of the Andes of Peru and Bolivia* AAPG Memoirs. (AAPG), 91–121.

Baby, P., Colletta, B., and Zubieta, D. (1995). Etude geometrique et experimentale d'un bassin transporte; exemple du synclinorium de l'Alto Beni (Andes centrales). *Bull. Société Géologique Fr.* 166, 797–811.

Bahlburg, H., Vervoort, J. D., Andrew DuFrane, S., Carlotto, V., Reimann, C., and Cárdenas, J. (2011). The U–Pb and Hf isotope evidence of detrital zircons of the Ordovician Ollantaytambo Formation, southern Peru, and the Ordovician provenance and paleogeography of southern Peru and northern Bolivia. *J. South Am. Earth Sci.* 32, 196–209. doi: 10.1016/j.jsames.2011.07.002.

Boekhout, F., Sempere, T., Spikings, R., Schaltegger, U., 2013. Late Paleozoic to Jurassic chronostratigraphy of coastal southern Peru: Temporal evolution of sedimentation along an active margin. J. South Am. Earth Sci. 47, 179–200. https://doi.org/10.1016/j.jsames.2013.07.003

Bookhagen, B., Strecker, M. R. 2018. Orographic barriers, high-resolution TRMM rainfall, and relief variations along the eastern Andes, *Geophys. Res. Lett.*,35, L06403, doi:10.1029/2007GL032011.

Boyer, S. E. (1992). "Geometric evidence for synchronous thrusting in the southern Alberta and northwest Montana thrust belts," in *Thrust Tectonics*, ed. K. R. McClay (Dordrecht: Springer Netherlands), 377–390. doi: 10.1007/978-94-011-3066-0_34.

Brandon, M. T. (1992). Decomposition of fission-track grain-age distributions. *Am. J. Sci.* 292, 535–564. doi: 10.2475/ajs.292.8.535.

Brandon, M. T. (1996). Probability density plot for fission-track grain-age samples. *Radiat. Meas.* 26, 663–676. doi: 10.1016/S1350-4487(97)82880-6.

Brandon, M. T. (2002). Decomposition of mixed grain age distributions using Binomfit. *Track* 24, 13–18.

Brandon, M. T., Roden-Tice, M. K., and Garver, J. I. (1998). Late Cenozoic

Campbell, K.E., Heizler, M., Frailey, C.D., Romero-Pittman, L. and Prothero, D.R., 2001. Upper Cenozoic chronostratigraphy of the southwestern Amazon Basin. Geology, 29(7): 595-598.

Campetella, C. M., and Vera, C. S. (2002). The influence of the Andes mountains on the South American low-level flow. *Geophys. Res. Lett.* 29, 7-1-7–4. doi: 10.1029/2002GL015451.

Carpenter, D. and Berumen, M., 1999. Geological and Geochemical Modeling of the Fold and Thrust Belt of the Southeastern, INGEPET Exploration and Exploration of Petroleum and Gas.

Chapple, W. M. (1978). Mechanics of thin-skinned fold-and-thrust belts. *GSA Bull.* 89, 1189–1198. doi: 10.1130/0016-7606(1978)89<1189:MOTFB>2.0.CO;2.

Chavez, C., Roddaz, M., Dantas, E. L., Santos, R. V., and Alván, A. A. (2022). Provenance of the Middle Jurassic-Cretaceous sedimentary rocks of the Arequipa Basin (South Peru) and implications for the geodynamic evolution of the Central Andes. *Gondwana Res.* 101, 59–76. doi: 10.1016/j.gr.2021.07.018.

Chavez, S. P. & Takahashi, K. (2017). Orographic rainfall hot spots in the Andes-Amazon transition according to the TRMM precipitation radar and in situ data. *Journal of Geophysical Research: Atmospheres, 122* (11), 5870-5882. https://doi.org/10.1002/2016JD026282

Cooperación Técnica Peruana-Alemana, 1982. Evaluación de las cuencas Ucayali y Madre de Dios.

Clark, A.H., Farrar, E., Kontak, D.J., Langridge, R.J., F, M.J.A., France, L.J., McBride, S.L., Woodman, P.L., Wasteneys, H.A., Sandeman, H.A., Archibald, D.A., 1990. Geologic and geochronologic constraints on the metallogenic evolution of the Andes of southeastern Peru. Econ. Geol. 85, 1520–1583. https://doi.org/10.2113/gsecongeo.85.7.1520

da Silva-Caminha, S.A.F., Jaramillo, C.A., Absy, M.L., 2010. Neogene palynology of the Solimões Basin, Brazilian Amazonia. *Palaeontogr. Abt. B* 13–79. https://doi.org/10.1127/palb/284/2010/13

Dahlen, F. A. (1984). Noncohesive critical Coulomb wedges: An exact solution. *J. Geophys. Res. Solid Earth* 89, 10125–10133. doi: 10.1029/JB089iB12p10125.

Dahlen, F. A. (1990). CRITICAL TAPER MODEL OF FOLD-AND-THRUST BELTS AND ACCRETIONARY WEDGES. *Annu. Rev. Earth Planet. Sci.* 18, 55–99. doi: 10.1146/annurev.ea.18.050190.000415.

Dahlen, F. A., Suppe, J., and Davis, D. (1984). Mechanics of fold-and-thrust belts and accretionary wedges: Cohesive Coulomb Theory. *J. Geophys. Res. Solid Earth* 89, 10087–10101. doi: 10.1029/JB089iB12p10087.

Dalmayrac, B., Laubacher, G., Marocco, R., Martinez, C., and Tomasi, P. (1980). La chaine hercynienne d'amerique du sud structure et evolution d'un orogene intracratonique. *Geol. Rundsch.* 69, 1–21. doi: 10.1007/BF01869020.

Dalmayrac, B., and Molnar, P. (1981). Parallel thrust and normal faulting in Peru and constraints on the state of stress. *Earth Planet. Sci. Lett.* 55, 473–481. doi: 10.1016/0012-821X(81)90174-6.

Davis, D., Suppe, J., and Dahlen, F. A. (1983). Mechanics of fold-and-thrust belts and accretionary wedges. *J. Geophys. Res. Solid Earth* 88, 1153–1172. doi: 10.1029/JB088iB02p01153.

DeCelles, P. G. (1994). Late Cretaceous-Paleocene synorogenic sedimentation and kinematic history of the Sevier thrust belt, northeast Utah and southwest Wyoming. *GSA Bull.* 106, 32–56. doi: 10.1130/0016-7606(1994)106<0032:LCPSSA>2.3.CO;2.

DeCelles, P. G., and Horton, B. K. (2003). Early to middle Tertiary foreland basin development and the history of Andean crustal shortening in Bolivia. *GSA Bull.* 115, 58–77. doi: 10.1130/0016-7606(2003)115<0058:ETMTFB>2.0.CO;2.

DeCelles, P. G., and Mitra, G. (1995). History of the Sevier orogenic wedge in terms of critical taper models, northeast Utah and southwest Wyoming. *GSA Bull.* 107, 454–462. doi: 10.1130/0016-7606(1995)107<0454:HOTSOW>2.3.CO;2.

Echavarria, L., Hernndez, R., Allmendinger, R., and Reynolds, J. (2003). Subandean thrust and fold belt of northwestern Argentina: Geometry and timing of the Andean evolution. *AAPG Bull.* 87, 965–985.

Espinoza, J. C., Garreaud, R., Poveda, G., Arias, P. A., Molina-Carpio, J., Masiokas, M., et al. (2020). Hydroclimate of the Andes Part I: Main Climatic Features. *Front. Earth Sci.* 8. Available at: https://www.frontiersin.org/article/10.3389/feart.2020.00064 [Accessed April 6, 2022].

Espurt, N., Barbarand, J., Roddaz, M., Brusset, S., Baby, P., Saillard, M., et al. (2011). A scenario for late Neogene Andean shortening transfer in the Camisea Subandean zone (Peru, 12°S): Implications for growth of the northern Andean Plateau. *Geol. Soc. Am. Bull.* 123, 2050–2068. doi: 10.1130/B30165.1.

Esteban, M. and Klappa, C., 1983. Carbonate depositional environments. AAPG Memoir, 33: 1-54.

Eude, A., Roddaz, M., Brichau, S., Brusset, S., Calderon, Y., Baby, P., et al. (2015). Controls on timing of exhumation and deformation in the northern Peruvian eastern Andean wedge as inferred from low-temperature thermochronology and balanced cross section. *Tectonics* 34, 2014TC003641. doi: 10.1002/2014TC003641.

Galbraith, R. F. (1988). Graphical Display of Estimates Having Differing Standard Errors. *Technometrics* 30, 271–281. doi: 10.2307/1270081.

Galbraith, R. F., and Green, P. F. (1990). Estimating the component ages in a finite mixture. *Int. J. Radiat. Appl. Instrum. Part Nucl. Tracks Radiat. Meas.* 17, 197–206. doi: 10.1016/1359-0189(90)90035-V.

Gautheron, C., Tassan-Got, L., 2009. A Monte Carlo approach to diffusion applied to noble gas/helium thermochronology. *Chemical Geology* 273, 212–224.

Gautheron, C., Espurt, N., Barbarand, J., Roddaz, M., Baby, P., Brusset, S., et al. (2013). Direct dating of thick- and thin-skin thrusts in the Peruvian Subandean zone through apatite (U–Th)/He and fission track thermochronometry. *Basin Res.* 25, 419–435. doi: 10.1111/bre.12012

Germeraad, J.H., Hopping, C.A., Muller, J., 1968. Palynology of tertiary sediments from tropical areas. *Rev. Palaeobot. Palynol., Palinology of Tertiary Sediments from Tropical Areas* 6, 189–348. https://doi.org/10.1016/0034-6667(68)90051-1

Gil Rodriguez, W., Baby, P., and Ballard, J.-F. (2001). Structure et contrôle paléogéographique de la zone subandine péruvienne. *Comptes Rendus Académie Sci. - Ser. IIA - Earth Planet. Sci.* 333, 741–748. doi: 10.1016/S1251-8050(01)01693-7.

Gil, W. F. (2001). Evolution latérale de la déformation d'un front orogénique : exemple des bassins subandins entre 0° et 16°S. Available at: http://www.theses.fr/2001TOU30045 [Accessed August 19, 2021].

Gutierrez, M., 1982. Evaluacion potencial petrolifero cuencas Huallaga, Ucayali y Madre de Dios. Zonacion bioestratigrafica del intervalo Cretacico superior-Tertiario inferior, Petroperu, Internal Report, Lima.

Hermoza, W. (2004). Dynamique tectono-sédimentaire et restauration séquentielle du rétro-bassin d'avant-pays des Andes centrales. *http://www.theses.fr*. Available at: http://www.theses.fr/2004TOU30134 [Accessed January 10, 2022].

Hoorn, C. 1993. Marine incursions and the influence of Andean tectonics on the Miocene depositional history of northwestern Amazonia: results of a palynostratigraphic study. *Palaeogeogrp. Palaeoclimatol. Palaeocol*, 105, 267-209.

Hoorn, C., Bogot´a-A, G.R., Romero-Baez, M., Lammertsma, E.I., Flantua, S.G.A., Dantas, E.L., Dino, R., do Carmo, D.A., Chemale, F., 2017. The Amazon at sea: Onset and stages of the Amazon River from a marine record, with special reference to Neogene plant turnover in the drainage basin. *Glob. Planet. Change* 153, 51–65. https://doi.org/10.1016/j.gloplacha.2017.02.005.

Hoorn, C., Kukla, T., Bogotá-Angel, G., van Soelen, E., González-Arango, C.,

Horton, B. K. (1999). Erosional control on the geometry and kinematics of thrust belt development in the central Andes. *Tectonics* 18, 1292–1304. doi: 10.1029/1999TC900051.

Horton, B. K. (2018b). Tectonic Regimes of the Central and Southern Andes: Responses to Variations in Plate Coupling During Subduction. *Tectonics* 37, 402–429. doi: 10.1002/2017TC004624.

Horton, B. K., and DeCelles, P. G. (1997). The modern foreland basin system adjacent to the Central Andes. *Geology* 25, 895–898. doi: 10.1130/0091-7613(1997)025<0895:TMFBSA>2.3.CO;2.

Horton, B. K., Capaldi, T. N., Perez, N, D., 2022. The role of flat slab subduction, ridge subduction, and tectonic inheritance in Andean deformation. *Geology* 50(9), 1007-1012. doi: https://doi.org/10.1130/G50094.1

Hovikoski, J., Räsänen, M., Gingras, M., Roddaz, M., Brusset, S., Hermoza, W., Pittman, L.R. and Lertola, K., 2005. Miocene semidiurnal tidal rhythmites in Madre de Dios, Peru. Geology, 33(3): 177-180.

Hovikoski, J., Gingras, M., Räsänen, M., Rebata, L.A., Guerrero, J., Ranzi, A., Melo, J., Romero, L., del Prado, H.N. and Jaimes, F., 2007b. The nature of Miocene Amazonian epicontinental embayment: High-frequency shifts of the low-gradient coastline. Geological Society of America Bulletin, 119(11-12):1506-1520.

Hovikoski, J., Räsänen, M., Gingras, M., Lopéz, S., Romero, L., Ranzi, A.and Melo, J., 2007c. Palaeogeographical implications of the Miocene Quendeque Formation (Bolivia) and tidally influenced strata in southwestern Amazonia. Science Direct, 243: 23-41.

Hurtado, C., Roddaz, M., Santos, R. V., Baby, P., Antoine, P.-O., and Dantas, E. L. (2018). Cretaceous-early Paleocene drainage shift of Amazonian rivers driven by Equatorial Atlantic Ocean opening and Andean uplift as deduced from the provenance of northern Peruvian sedimentary rocks (Huallaga basin). *Gondwana Res.* 63, 152–168. doi: 10.1016/j.gr.2018.05.012.

Insel, N., Poulsen, C. J., and Ehlers, T. A. (2010). Influence of the Andes Mountains on South American moisture transport, convection, and precipitation. *Clim. Dyn.* 35, 1477–1492. doi: 10.1007/s00382-009-0637-1.

Jacobsen, S.B. and Wasserburg, G., 1980. Sm-Nd isotopic evolution of chondrites. Earth and Planetary Science Letters. 50(1): 139-155.

Jackson S., Pearson N.J., Griffin W. and Belousova E.A. (2004) The application of laser ablation-inductively coupled plasma-mass spectrometry to in situ U-Pb zircon geochronology. Chemical Geology, 211, 47-69.

Jaramillo, C.A., Rueda, M., Torres, V., 2011. A palynological zonation for the Cenozoic of the Llanos and Llanos Foothills of Colombia. Palynology 35, 46–84. https://doi.org/10.1080/01916122.2010.515069

Jaramillo, C. A., Rueda, M., and Torres, V. (2011). A palynological zonation for the Cenozoic of the Llanos and Llanos Foothills of Colombia. *Palynology* 35, 46–84. doi: 10.1080/01916122.2010.515069.

Jo, H., Rhee, C. and Chough, S., 1997. Distinctive characteristics of a streamflow-dominated alluvial fan deposit: Sanghori area, Kyongsang Basin (Early Cretaceous), southeastern Korea. Sedimentary Geology, 110(1): 51-79.

Ketcham, R. A. (2005). Forward and Inverse Modeling of Low-Temperature Thermochronometry Data. *Rev. Mineral. Geochem.* 58, 275–314. doi: 10.2138/rmg.2005.58.11.

Ketcham, R. A., A. Carter, R. Donelick, J. Barbarand, and A. Hurford (2007), Improved modeling of fission-track annealing in apatite, Am. Mineral., 92, 799–810, doi:10.2138/am.2007.2281.

Kontak, D. J., Clark, A. H., Farrar, E., Archibald, D. A., and Baadsgaard, H. (1990). Late Paleozoic-early Mesozoic magmatism in the Cordillera de Carabaya, Puno, southeastern Peru: Geochronology and petrochemistry. *J. South Am. Earth Sci.* 3, 213–230. doi: 10.1016/0895-9811(90)90004-K.

Kontak, D.J., Clark, A.H., Farrar, E., Strong, D.F., 1985. The rift-associated Permo-Triassic magmatism of the Eastern Cordillera: a precursor to the Andean orogeny. Rift-Assoc. Permo-Triassic Magmat. East. Cordill. Precursor Andean Orogeny, 36–44.

Lacan, F., 2002. Masses d'eau des Mers Nordiques et de l'Atlantique Subarctique tracées par les isotopes du néodyme, Université Paul Sabatier-Toulouse III.

Laubacher, Gérard, and Megard, F. (1985). “The Hercynian basement: a review:,” in *Magmatism at a Plate Edge: The Peruvian Andes* (Pitcher, W.S., Atherton, M.P., Cobbing, E.J., and Beckinsale, R.D.), 29–35.

Lease, R. O., and Ehlers, T. A. (2013). Incision into the Eastern Andean Plateau During Pliocene Cooling. *Science* 341, 774–776. doi: 10.1126/science.1239132.

Lenters, J. D., and Cook, K. H. (1995). Simulation and Diagnosis of the Regional Summertime Precipitation Climatology of South America. *J. Clim.* 8, 2988–3005.

Leturmy, P., Mugnier, J. L., Vinour, P., Baby, P., Colletta, B., and Chabron, E. (2000). Piggyback basin development above a thin-skinned thrust belt with two detachment levels as a function of interactions between tectonic and superficial mass transfer: the case of the Subandean Zone (Bolivia). *Tectonophysics* 320, 45–67.

Loewy, J. N., Connely, Dalziel, I. W. D. 2004. An orphaned basement block: The Arequipa-Antofalla Basement of the central Andean margin of South America. GSA Bull., 116, pp. 171-187. Doi:10.1130/B25226.1

Louterbach, M. (2014). Propagation du front orogénique Subandin et réponse sédimentaire associée dans le bassin d'avant-pays amazonien (Madre de Dios, Pérou). Available at: http://thesesups.ups-tlse.fr/2530/

Louterbach, M., Roddaz, M., Antoine, P.-O., Marivaux, L., Adnet, S., Bailleul, J., et al. (2018b). Provenance record of late Maastrichtian–late Palaeocene Andean Mountain building in the Amazonian retroarc foreland basin (Madre de Dios basin, Peru). *Terra Nova* 30, 17–23. doi: 10.1111/ter.12303.

Margirier, A., Strecker, M. R., Reiners, P. W., Thomson, S. N., Casado, I., George, S. W. M., & Alvarado, A. (2023). Late Miocene exhumation of the Western Cordillera, Ecuador, driven by increased coupling between the subducting Carnegie Ridge and the South American continent. *Tectonics*, 42, e2022TC007344. https://doi.org/10.1029/2022TC007344

Marivaux, L., Salas-Gismondi, R., Tejada, J., Billet, G., Louterbach, M., Vink, J., et al. (2012a). A platyrrhine talus from the early Miocene of Peru (Amazonian Madre de Dios Sub-Andean Zone). *J. Hum. Evol.* 63, 696–703. doi: 10.1016/j.jhevol.2012.07.005.

Marivaux, L., Salas-Gismondi, R., Tejada, J., Billet, G., Louterbach, M., Vink, J., et al. (2012b). A platyrrhine talus from the early Miocene of Peru (Amazonian Madre de Dios Sub-Andean Zone). *J. Hum. Evol.* 63, 696–703. doi: 10.1016/j.jhevol.2012.07.005.

Marocco, R. (1978). Estudio geológico de la Cordillera de Vilcabamba-.

McQuarrie, N., and DeCelles, P. (2001). Geometry and structural evolution of the central Andean backthrust belt, Bolivia. *Tectonics* 20, 669–692. doi: 10.1029/2000TC001232.

McQuarrie, N., Ehlers, T. A., Barnes, J. B., and Meade, B. (2008b). Temporal variation in climate and tectonic coupling in the central Andes. *Geology* 36, 999–1002. doi: 10.1130/G25124A.1.

Megard, F. (1978). *Etude geologique des Andes du Perou central; contribution a l'etude geologique des Andes N*. Memoires ORSTOM.

Mégard, F. (1984). The Andean orogenic period and its major structures in central and northern Peru. *J. Geol. Soc.* 141, 893–900. doi: 10.1144/gsjgs.141.5.0893.

Miall, A.D., 1996. The geology of fluvial deposits: sedimentary facies, basin analysis, and petroleum geology. Springer-Verlag Inc Berlin, 582 pp.

Mišković, A., Spikings, R. A., Chew, D. M., Košler, J., Ulianov, A., and Schaltegger, U. (2009). Tectonomagmatic evolution of Western Amazonia: Geochemical characterization and zircon U-Pb geochronologic constraints from the Peruvian Eastern Cordilleran granitoids. *Geol. Soc. Am. Bull.* 121, 1298–1324. doi: 10.1130/B26488.1.

Mitra, G., and Sussman, A. J. (1997). Structural evolution of connecting splay duplexes and their implications for critical taper: an example based on geometry and kinematics of the Canyon Range culmination, Sevier Belt, Central Utah. *J. Struct. Geol.* 19, 503–521. doi: 10.1016/S0191-8141(96)00108-3.

Mobil Oil Corporation, 1998. Phase I Technical Synthesis Tambopata Lot 78, Peru.

Moizinho, G. R., Vieira, L. C., Santos, R. V., Nogueira, A. C. R., Dantas, E. L., Roddaz, M. (2022). Provenance of Miocene-Pleistocene siliciclastic deposits in the Eastern Amazonia coast (Brazil) and paleogeographic implications. *Palaeogeogrp. Palaeoclimatol. Palaeocol*. 587, 110799.

Mora, A., Baby, P., Roddaz, M., Parra, M., Brusset, S., Hermoza, W., et al. (2011). "Tectonic History of the Andes and Sub-Andean Zones: Implications for the Development of the Amazon Drainage Basin," in *Amazonia: Landscape and Species Evolution* (Wiley-Blackwell), 38–60. doi: 10.1002/9781444306408.ch4.

Mora, A., Ketcham, R. A., Higuera-Diaz, I. C., Bookhagen, B., Jimenez, L., and Rubiano, J. (2014). Formation of passive-roof duplexes in the Colombian Subandes and Peru. *Lithosphere* 6, 456–472. doi: 10.1130/L340.1.

Oliveros, V., Labbé, M., Rossel, P., Charrier, R., Encinas, A., 2012. Late Jurassic paleogeographic evolution of the Andean back-arc basin: New constrains from the Lagunillas Formation, northern Chile (27°30'–28°30'S). J. South Am. Earth Sci. 37, 25–40. https://doi.org/10.1016/j.jsames.2011.12.005

Oncken, O., Boutelier, D., Dresen, G., Schemmann, K.(2012). Strain accumulation controls failure of a plate boundary zone: Linking deformation of the Central Andes and lithosphere mechanics, *Geochem. Geophys. Geosyst.*,13, Q12007, doi:10.1029/2012GC004280.

Parra, M., Mora, A., Jaramillo, C., Torres, V., Zeilinger, G., Strecker, M. R. 2010. Tectonic controls on Cenozoic foreland basin development in the north-eastern Andes, Colombia. Basin Res. 22(6), 874-903. https://doi.org/10.1111/j.1365-2117.2009.00459.x

Perez, N. D., and Horton, B. K. (2014). Oligocene-Miocene deformational and depositional history of the Andean hinterland basin in the northern Altiplano plateau, southern Peru. *Tectonics* 33, 1819–1847. doi: 10.1002/2014TC003647.

Perez, N. D., Horton, B. K., McQuarrie, N., Stubner, K., and Ehlers, T. A. (2016). Andean shortening, inversion and exhumation associated with thin- and thick-skinned deformation in southern Peru. *Geol. Mag.* 153, 1013–1041. doi: 10.1017/S0016756816000121.

Pérez-Consuegra, N., Hoke, G. D., Mora, A., Fitzgerald, P., Sobel, E. R., Sandoval, J. R., et al. (2021). The Case for Tectonic Control on Erosional Exhumation on the Tropical Northern Andes Based on Thermochronology Data. *Tectonics* 40, e2020TC006652. doi: 10.1029/2020TC006652.

Petrus, J.A., Kamber, B.S., 2012. VizualAge: a Novel Approach to Laser Ablation ICP-MS UPb Geochronology Data Reduction. Geostand. Geoanalytical Res. 36, 247–270. https:// doi.org/10.1111/j.1751-908X.2012.00158.x

Powers, M.C., 1953, A New Roundness Scale for Sedimentary Particles: *J. Sed. Res.,* 23117–119, doi: 10.1306/D4269567-2B26-11D7-8648000102C1865D.

Reimann, C. R., Bahlburg, H., Kooijman, E., Berndt, J., Gerdes, A., Carlotto, V., et al. (2010). Geodynamic evolution of the early Paleozoic Western Gondwana margin 14°–17°S reflected by the detritus of the Devonian and Ordovician basins of southern Peru and northern Bolivia. *Gondwana Res.* 18, 370–384. doi: 10.1016/j.gr.2010.02.002.

Retallack, G., 1997. Palaeosols in the upper Narrabeen group of New South Wales as evidence of Early Triassic palaeoenvironments without exact modern analogues*. Australian Journal of Earth Sciences, 44(2): 185-201.

Ridgway, K.D. and DeCelles, P.G., 1993. Stream-dominated alluvial fan and lacustrine depositional systems in Cenozoic strike-slip basins, Denali fault system, Yukon Territory, Canada. Sedimentology, 40(4): 645-666.

Roddaz, M., Viers, J., Brusset, S., Baby, P., and Hérail, G. (2005b). Sediment provenances and drainage evolution of the Neogene Amazonian foreland basin. *Earth Planet. Sci. Lett.* 239, 57–78. doi: 10.1016/j.epsl.2005.08.007.

Roddaz, M., Brusset, S., Baby, P. and Hérail, G., 2006. Miocene tidal influenced sedimentation to continental Pliocene sedimentation in the forebulge–backbulge depozones of the Beni–Mamore foreland Basin (northern Bolivia). Journal of South American Earth Sciences, 20(4): 351-368.

Roddaz, M., Hermoza, W., Mora, A., Baby, P., Parra, M., Christophoul, F., Brusset, S. and Espurt, N., 2010. Cenozoic sedimentary evolution of the Amazonian foreland basin system, pp. 61-88.

Rousseau, T.C.C., Roddaz, M., Moquet, J.-S., Handt Delgado, H., Calves, G., Bayon, G., 2019. Controls on the geochemistry of suspended sediments from large tropical South American rivers (Amazon, Orinoco, and Maroni). Chem. Geol. 522, 38–54. https://doi.org/10.1016/j.chemgeo.2019.05.027

Sanchez, C., 2012. Reconstitution de l'exhumation cénozoïque des Andes Centrales à partir de l'étude de la provenance des sédiments du bassin amazonien (analyses géochimique (majeurs, trace et isotopie Nd-Sr) et minéralogique (RX et minéraux lourds) (Master thesis). Univeristé Paul Sabatier Toulouse 3, Toulouse.

Santos, R.V., Sondag, F., Cochonneau, G., Lagane, C., Brunet, P., Hattingh, K., Chaves, J.G.S., 2015. Source area and seasonal 87 Sr/ 86 Sr variations in rivers of the Amazon basin: AMAZON RIVERS SOURCE SEDIMENTS. Hydrol. Process. 29, 187–197. https://doi.org/10.1002/hyp.10131.

Sepulchre, P., Sloan, L. C., and Fluteau, F. (2009). "Modelling the Response of Amazonian Climate to the Uplift of the Andean Mountain Range," in *Amazonia: Landscape and Species Evolution* (John Wiley & Sons, Ltd), 211–222. doi: 10.1002/9781444306408.ch13.

Sempere, T., Carlier. C., Soler, P., Fornari, M., Carlotto, V., Jacay, J., Arispe, O., Néraudeau, D., Cárdenas, J., Rosas, S., Jiménez, N. 2002. Late Permian-Middle Jurassic lithospheric thinning in Peru and Bolivia, and it's bearing on Andean-age tectonics. Tectonophys., Andean Geodyn. ISAG, 4 (345), pp. 153-181. Doi: 10.1016/S0040-1951(01)00211-6

Sláma, J., et al., 2008. Plezovice zircon A new natural reference material for U–Pb and Hf isotopic microanalysis, Chemical Geology, Chemical Geology, 249, p 1-35, doi:10.1016/j.chemgeo.2007.11.005

Soler, P., Bonhomme, M.G., 1990. Relation of magmatic activity to plate dynamics in central Peru from Late Cretaceous to present. https://doi.org/10.1130/SPE241-p173.

Spencer, C. J., Kirkland, C. L., Taylor, R. J. M. 2016. Strategies towards statistically robust interpretations of *in situ* U-Pb zircon geochronology. *Geosc. Front.* 7(4), 581-589.

Spikings, R., Reitsma, M. J., Boekhout, F., Mišković, A., Ulianov, A., Chiaradia, M., et al. (2016). Characterisation of Triassic rifting in Peru and implications for the early disassembly of western Pangaea. *Gondwana Res.* 35, 124–143. doi: 10.1016/j.gr.2016.02.008.

Sundell, K.E., Saylor, J.E., Lapen, T.J. *et al.* Implications of variable late Cenozoic surface uplift across the Peruvian central Andes. *Sci Rep* **9**, 4877 (2019). https://doi.org/10.1038/s41598-019-41257-3

Turner, P., 1980. Continental red beds. Elsevier.

Uba, C.E., Heubeck, C. and Hulka, C., 2005. Facies analysis and basin architecture of the Neogene Subandean synorogenic wedge, southern Bolivia. Sedimentary Geology, 180: 91-123.

Uba, C.E., Heubeck, C. and Hulka, C., 2006. Evolution of the late Cenozoic Chaco foreland basin, Southern Bolivia. Basin Research, 18(2): 145-170.

Uba, C. E., Kley, J., Strecker, M. R., and Schmitt, A. K. (2009a). Unsteady evolution of the Bolivian Subandean thrust belt: The role of enhanced erosion and clastic wedge progradation. *Earth Planet. Sci. Lett.* 281, 134–146. doi: 10.1016/j.epsl.2009.02.010.

Uba, C. E., Kley, J., Strecker, M. R., and Schmitt, A. K. (2009b). Unsteady evolution of the Bolivian Subandean thrust belt: The role of enhanced erosion and clastic wedge progradation. *Earth Planet. Sci. Lett.* 281, 134–146. doi: 10.1016/j.epsl.2009.02.010.

Valdivia, H., 1974. Estratigrafia de la Faja Subandina de la region de Madre de Dios.

van Soelen, E.E., Kim, J.-H., Santos, R.V., Dantas, E.L., Vasconcelos de Almeida, F., Pires, J.P., Roddaz, M., Sinninghe Damst´e, J.S., 2017. A 30 Ma history of the Amazon River inferred from terrigenous sediments and organic matter on the Ceará rise. Earth Planet. Sci. Lett. 474, 40–48. https://doi.org/10.1016/j.epsl.2017.06.025.

Vermeesch, P. (2013). Multi-sample comparison of detrital age distributions. *Chem. Geol.* 341, 140–146. doi: 10.1016/j.chemgeo.2013.01.010.

Vermeesch, P. (2018). Dissimilarity measures in detrital geochronology. *Earth-Sci. Rev.* 178, 310–321. doi: 10.1016/j.earscirev.2017.11.027.

Vermeesch, P., Resentini, A., and Garzanti, E. (2016). An R package for statistical provenance analysis. *Sediment. Geol.* 336, 14–25. doi: 10.1016/j.sedgeo.2016.01.009.

Viers, J., Roddaz, M., Filizola, N., Guyot, J.-L., Sondag, F., Brunet, P., Zouiten, C., Boucayrand, C., Martin, F., Boaventura, G.R., 2008. Seasonal and provenance controls on Nd-Sr isotopic compositions of Amazon rivers suspended sediments and implications for Nd and Sr fluxes exported to the Atlantic Ocean. Earth Planetary Science Letters. 274, 511–523.

Wiedenbeck, M., Alle, P., Corfu, F., Grif fin, W.L., Meier, M., Oberli, F., Von Quadt, A., Roddick, J.C., Spiegel, W., 1995. Three natural zircon standards for U-ThePb, Lu-Hf, trace element and REE analysis. Geostand. Newsl. 19, 1-23.

Wright, V. and Tucker, M., 1991. Calcretes. Reprint Series Volume 2 of the International Association of Sedimentologists. Blackwell Scientific Publications.

Zamora, G., Louterbach, M., and Arriola, P. (2019). “Chapter 12 - Structural controls along the Peruvian Subandes,” in *Andean Tectonics*, eds. B. K. Horton and A. Folguera (Elsevier), 333–362. doi: 10.1016/B978-0-12-816009-1.00015-0.

Zavaleta, A.G., Hauser, N., Roddaz, M., Gonçalves, G.O., González, P.A., Baby, P., Reimold, W.U., Puma, F., Bravo, P., and Humerez, M., 2023, Provenance of Devonian-Carboniferous sedimentary rocks of the Tarija Basin, southern Bolivia:

Implications for the geodynamic evolution of the southwestern margin of Gondwana: GSA Bulletin, https://doi.org/10.1130/B36701.1.

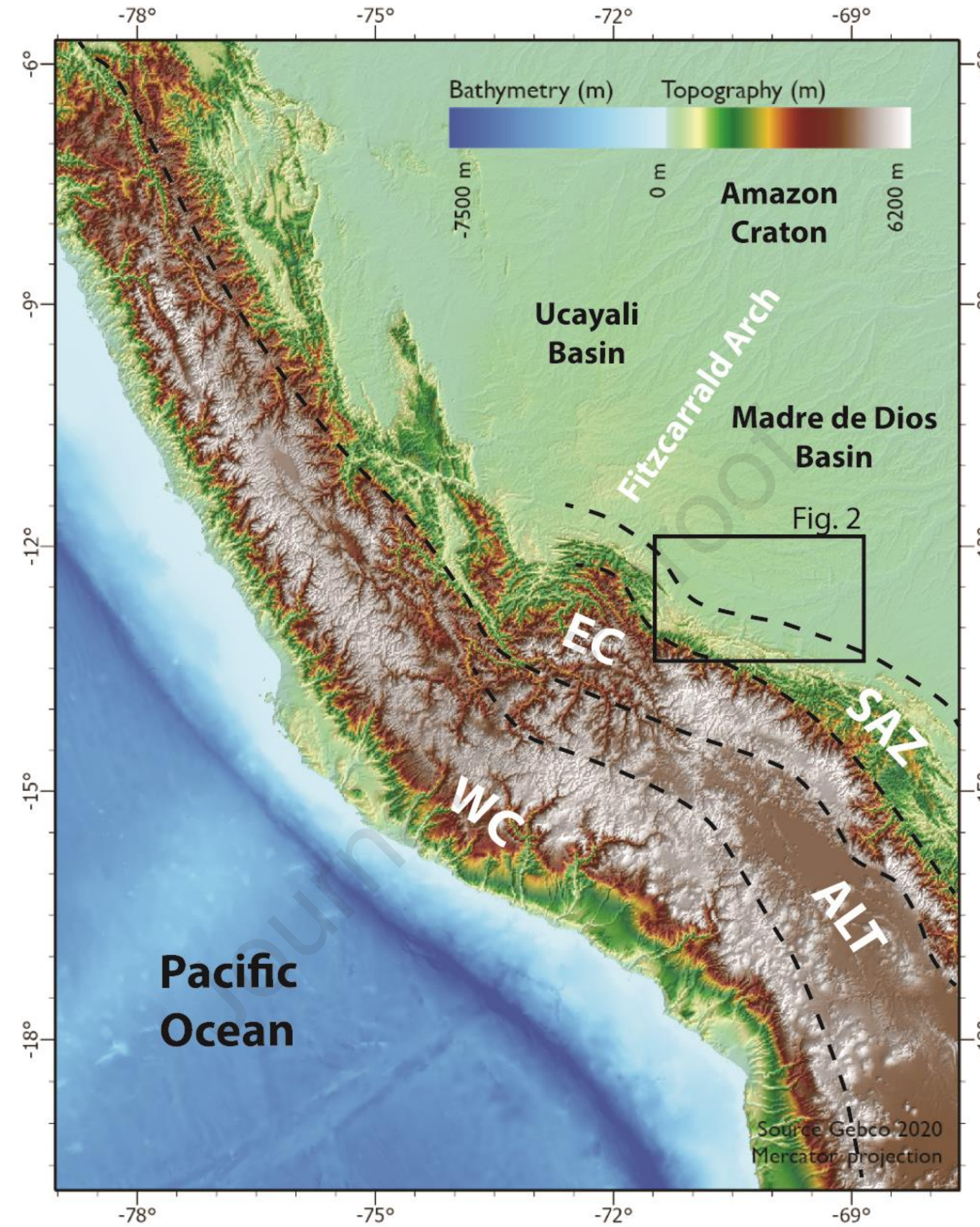

Figure 1. Topographic and bathymetric map of the central Andes showing the location of the studied area (thick black outline, Figure 2).

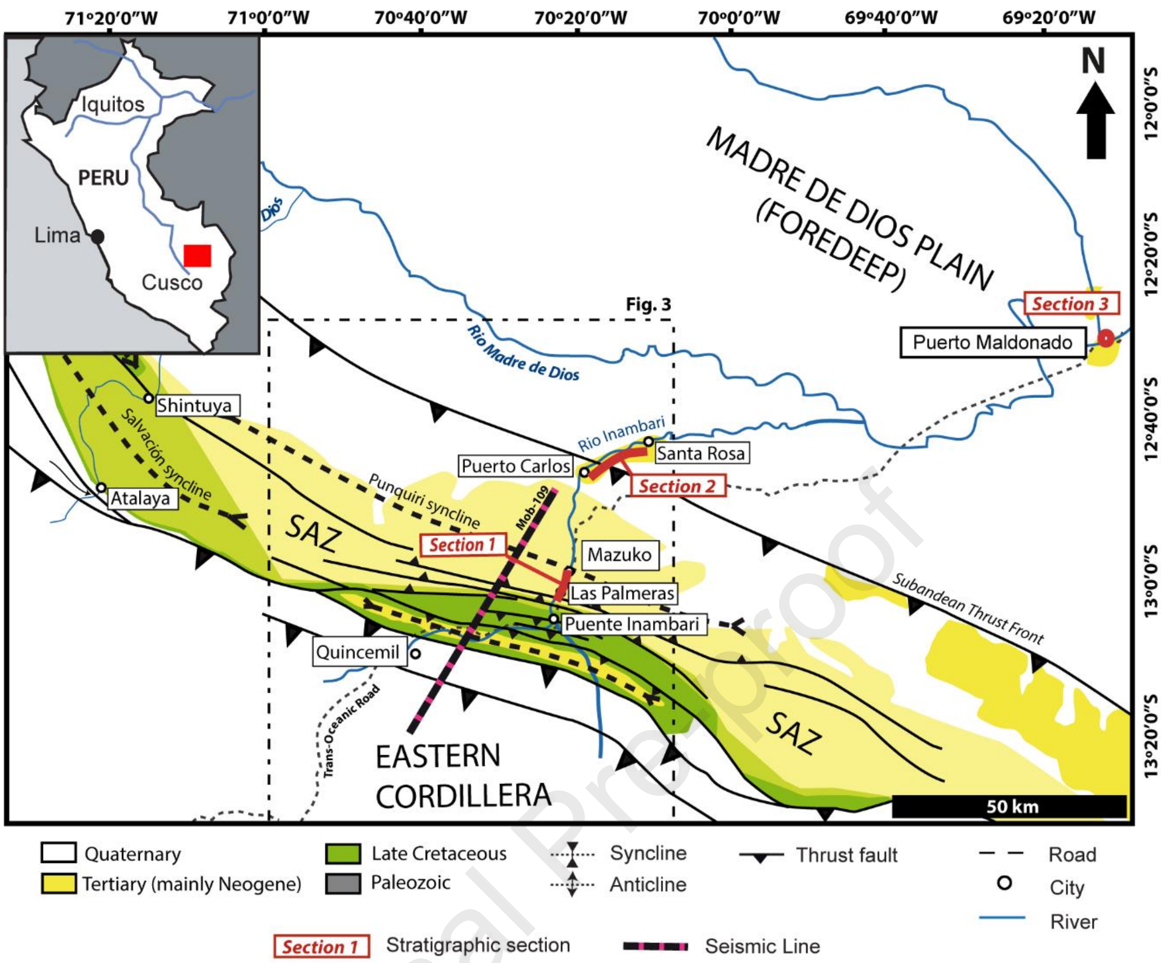

Figure 2. Simplified geological and structural map of the Madre de Dios foreland basin. The sedimentary sections described in this study are located along the Inambari River in the SAZ (Sections 1 and 2) and in Puerto Maldonado for the foredeep zone (Section 3). The seismic line MOB-109 utilized to interpret the Inambari transect is represented by the black, pink-dashed line.

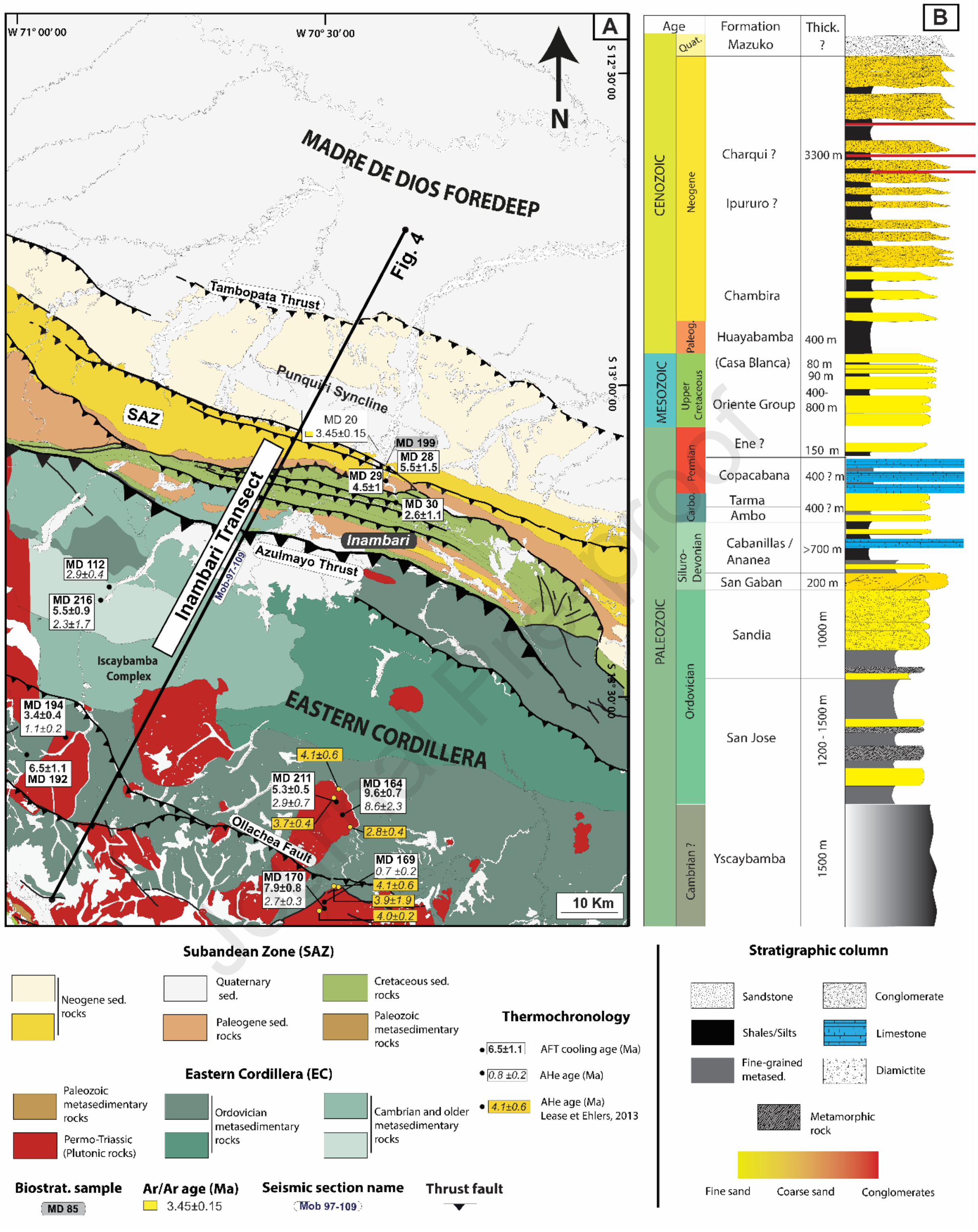

Figure 3. A) Geological map of the study area (modified after INGEMMET) with the main section. New biostratigraphic and thermochronological (AFT and AHe ages). **B)** Synthetic sedimentary column for the SAZ of the Madre de Dios foreland basin. Thickness and lithologies are taken from (Gil Rodriguez et al., 2001; Gil Rodriguez, 2002; Hermoza, 2004; Louterbach, 2014) and confidential reports. Simplified from Louterbach (2014).

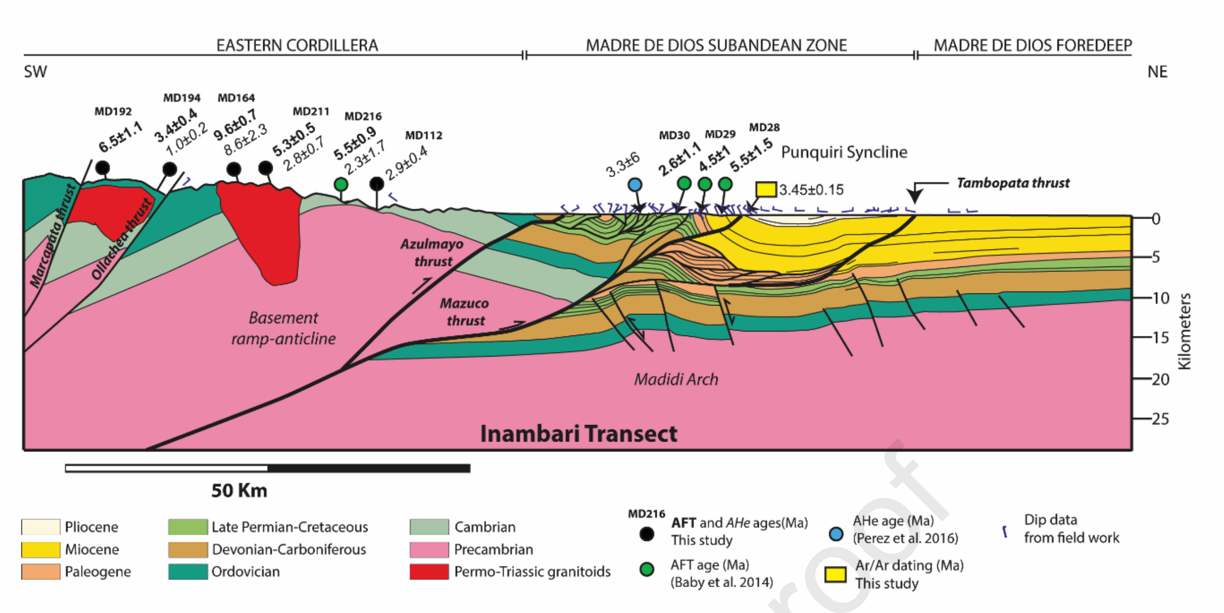

Figure 4. Inambari structural cross-section interpreted in depth. See Figure 3 for location. This section has been constructed using field data and MOB-97-109 and MD-56 seismic lines. Local geochronological constraints, as well as nearby thermochronological results, have been projected onto this section (modified after Baby et al., 2018b).

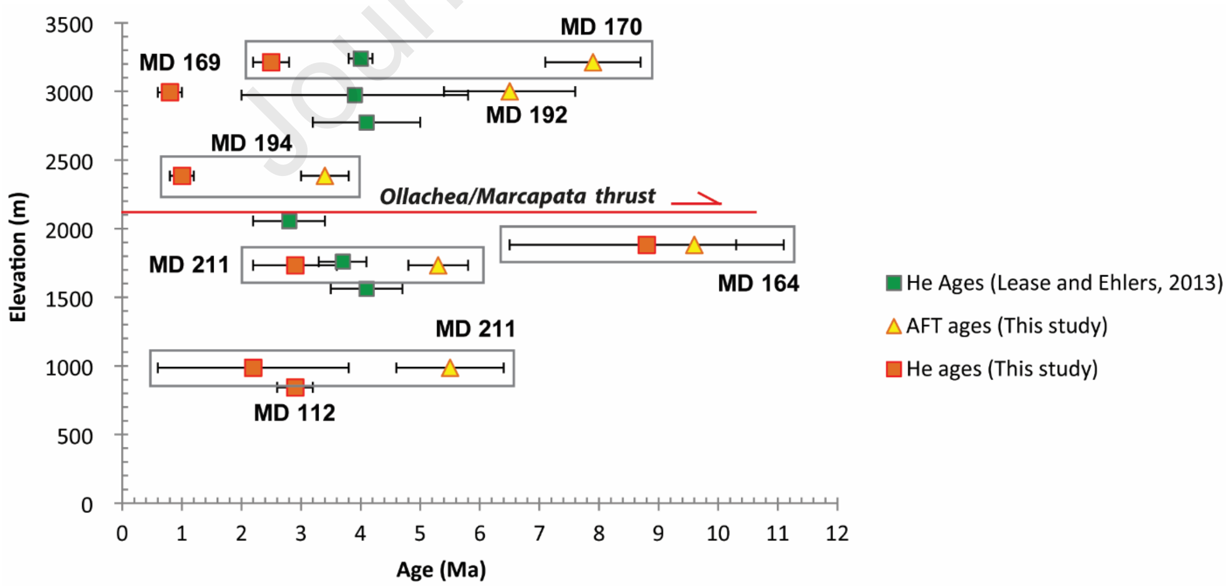

Figure 5. A) Cooling ages versus elevation. AHe, apatite (U-Th)/He; AFT, apatite Fission Track; AHe and AFT age errors are at 1σ standard for Eastern Cordillera samples.

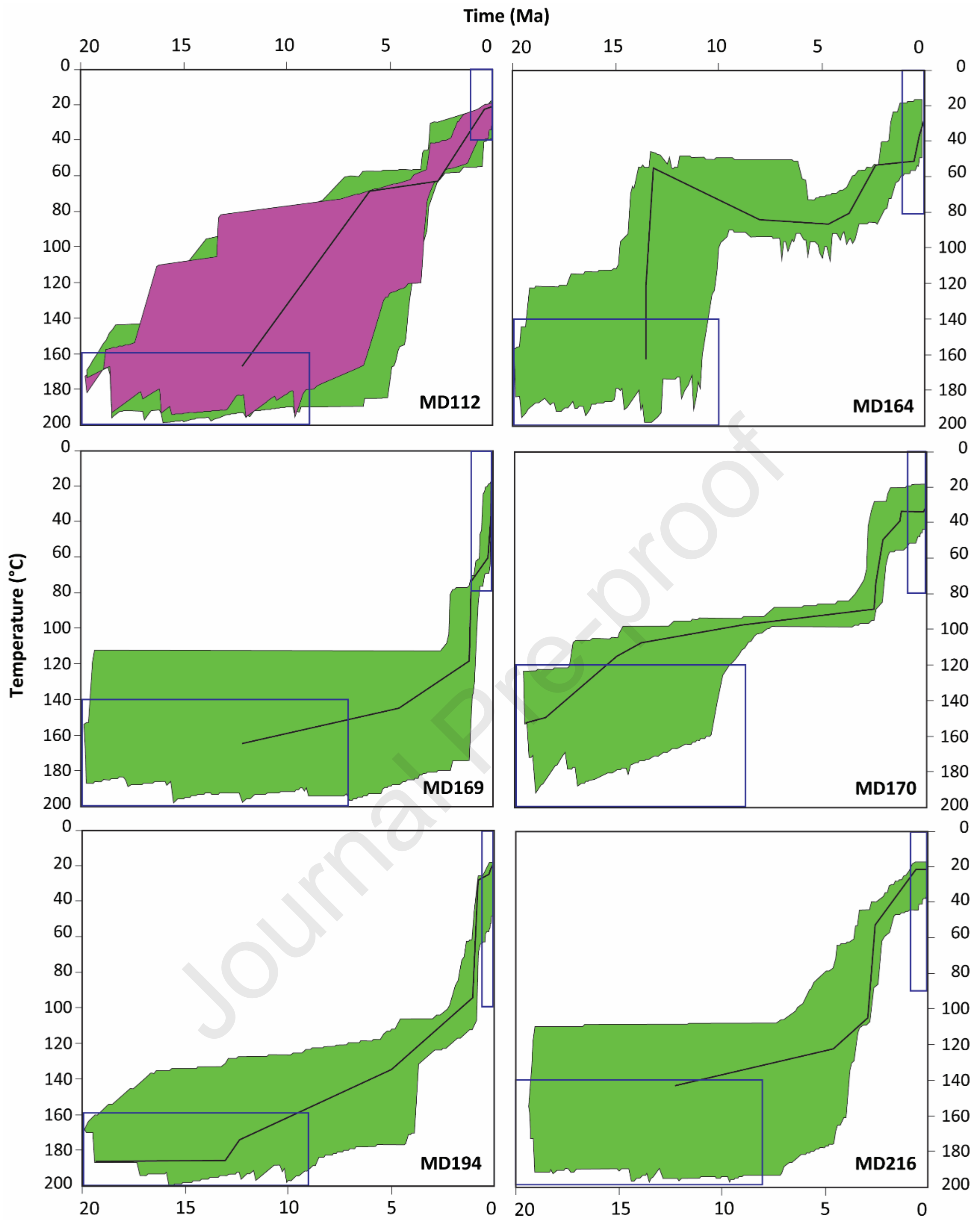

Figure 6. Modeled t-T paths for the crystalline EC samples (MD 112, MD164, MD169, MD170, MD194, and MD216) using 'HeFTy' software (see section 3.1.1. Thermal Modeling for detail on data input). Green: Thermal history with an acceptable fit (criterion of 0.05). Purple: Thermal history with a good fit (criterion of 0.5). Black line: best-fit models. Note that MD112, 164,169, 170, 194, 211, and 216 records almost all the same exhumation histories with a main period of exhumation between 1 and 3 Ma

while before the samples seem to stay in the PAZ during a long period of time (probably at least 4-5 Myr).

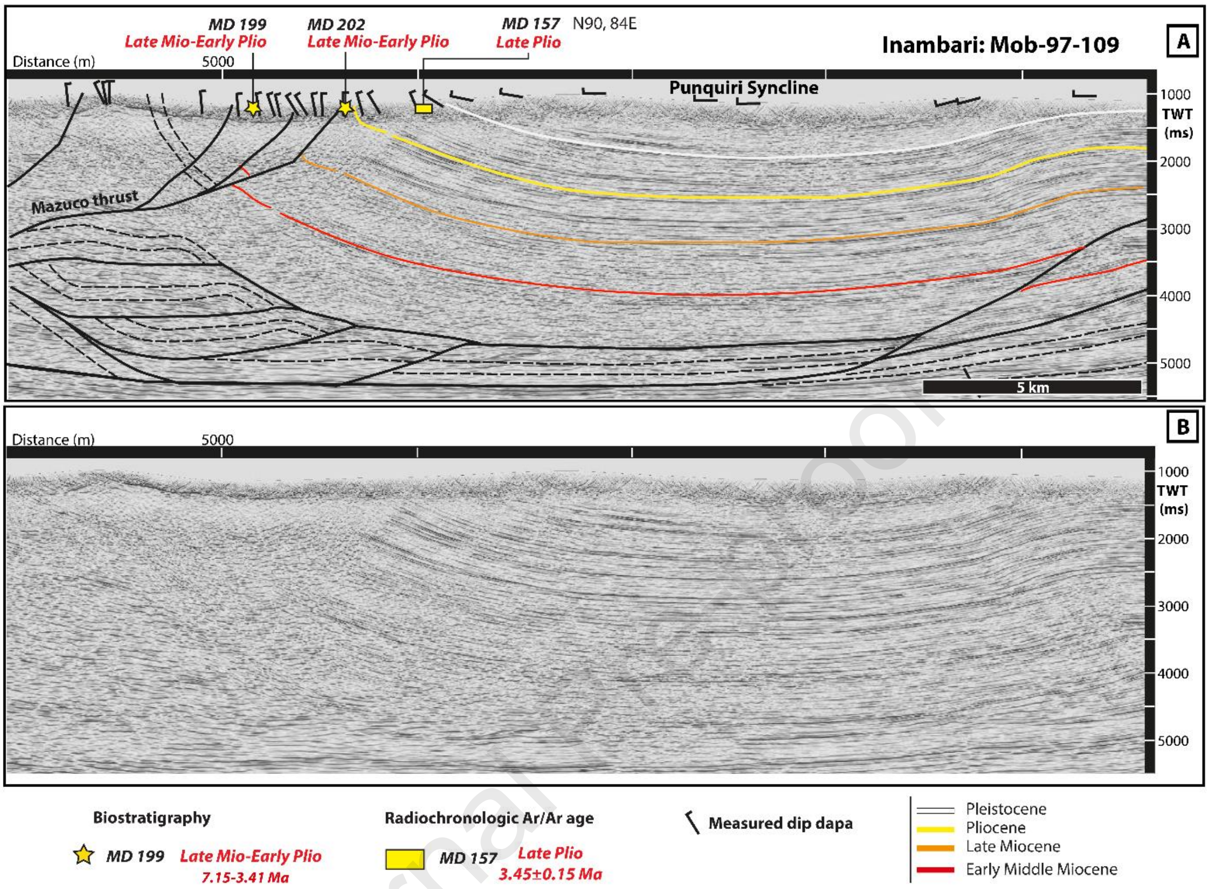

Figure 7. A) Interpreted profile of seismic section MOB-97-109 (see figures 2 and 3 for location) illustrating the sedimentary infilling of the Punquiri syncline (modified from Louterbach 2014). Dated outcrops were projected onto the seismic profile. The structural style of the SAZ duplex has been simplified. Dip values of analyzed outcrops projected onto the seismic line (black thick hyphens) show a progressive decrease toward the center of the syncline indicating syntectonic sedimentation associated with the duplex growth and Punquiri syncline formation (i.e., “growth strata deposits”); Late Mio: Late Miocene; Early Plio: Early Pliocene. B) Non-interpreted seismic line MOB-97-109.

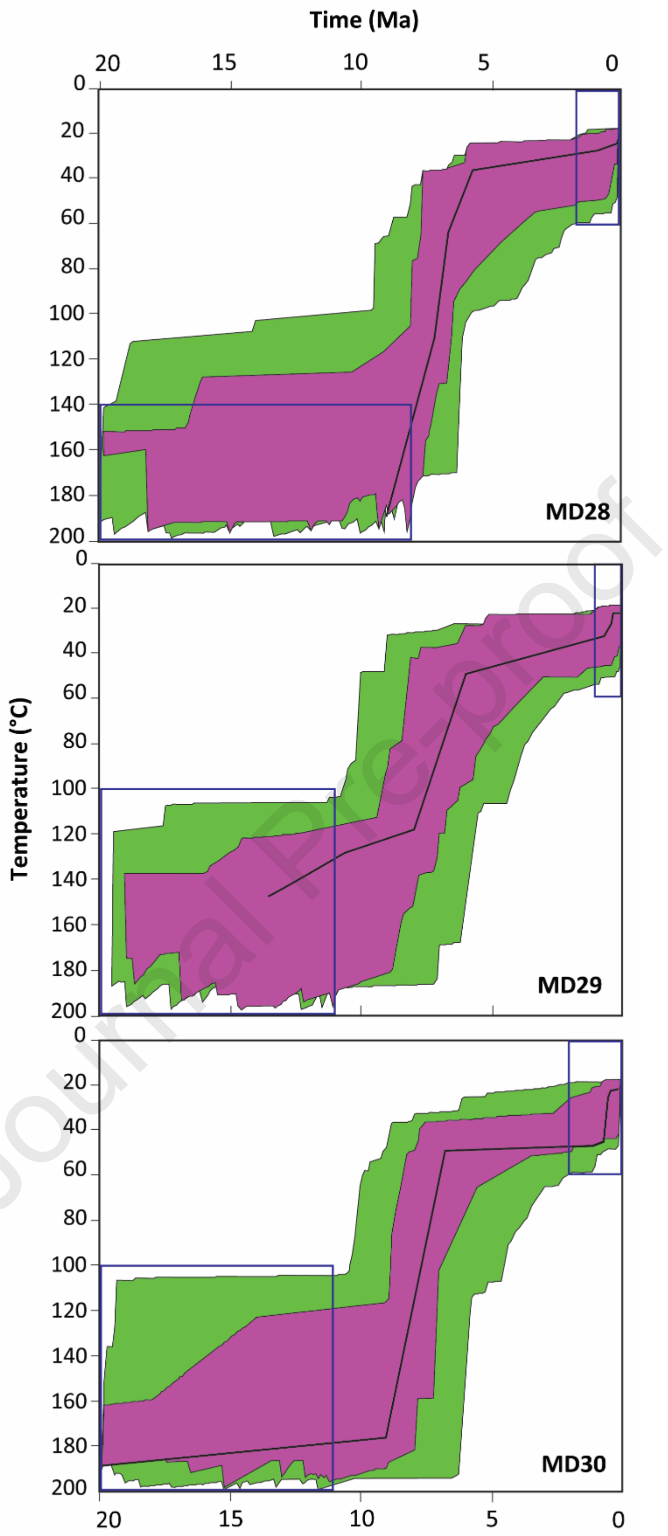

Figure 8. Modeled t-T paths for the SAZ samples (MD 30 (Cretaceous, SAZ), MD 29 (Cretaceous, SAZ) and MD 28 (Paleogene? SAZ) samples, using 'HeFTy' program (see section 3.1.1. Thermal Modeling for detail). Green: Thermal history with an acceptable fit (criterion of 0.05). Purple: Thermal history with a good fit (criterion of 0.5). Black line: best-fit models.

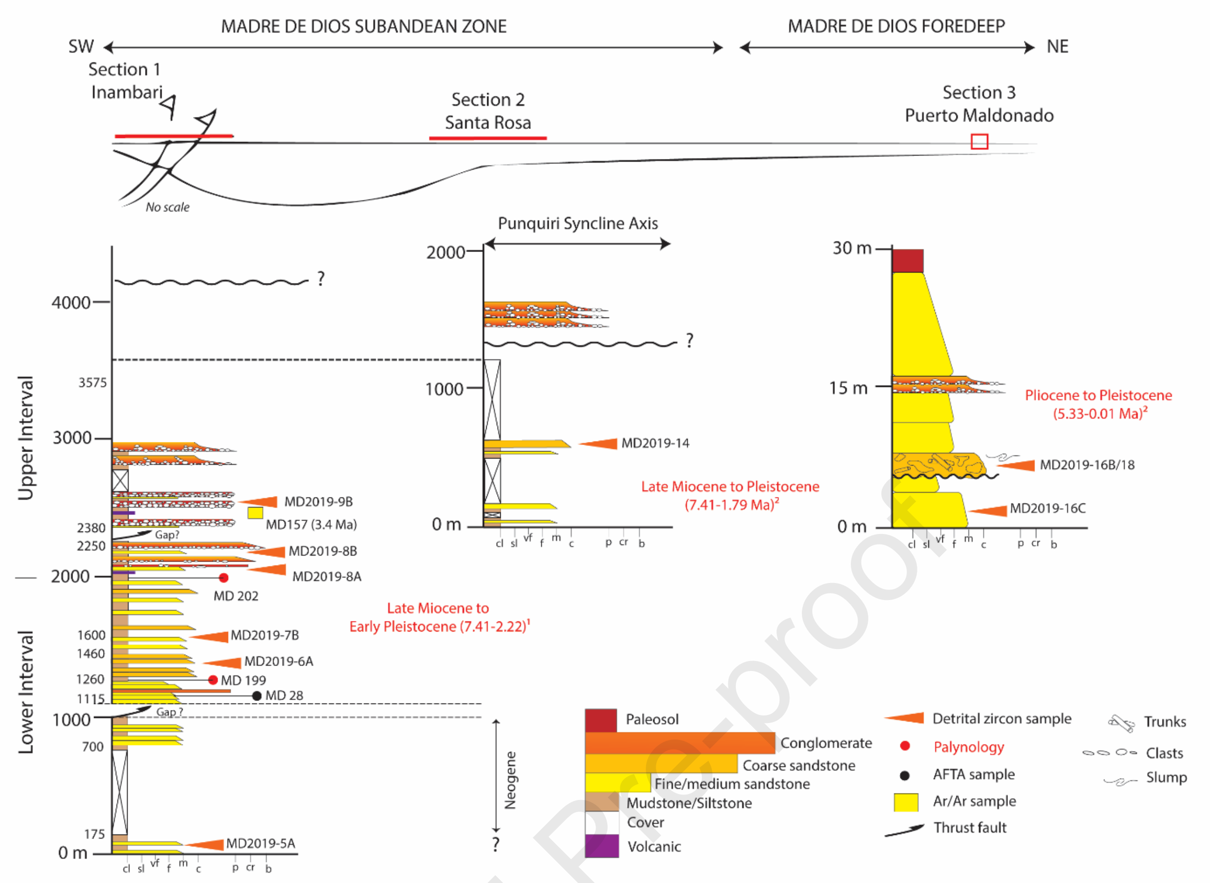

Figure 9. Simplified stratigraphic sections for the Neogene deposits in the Inambari Transect of the Madre de Dios Basin. Biostratigraphic ages are from [1]This work and [2] Louterbach (2014).

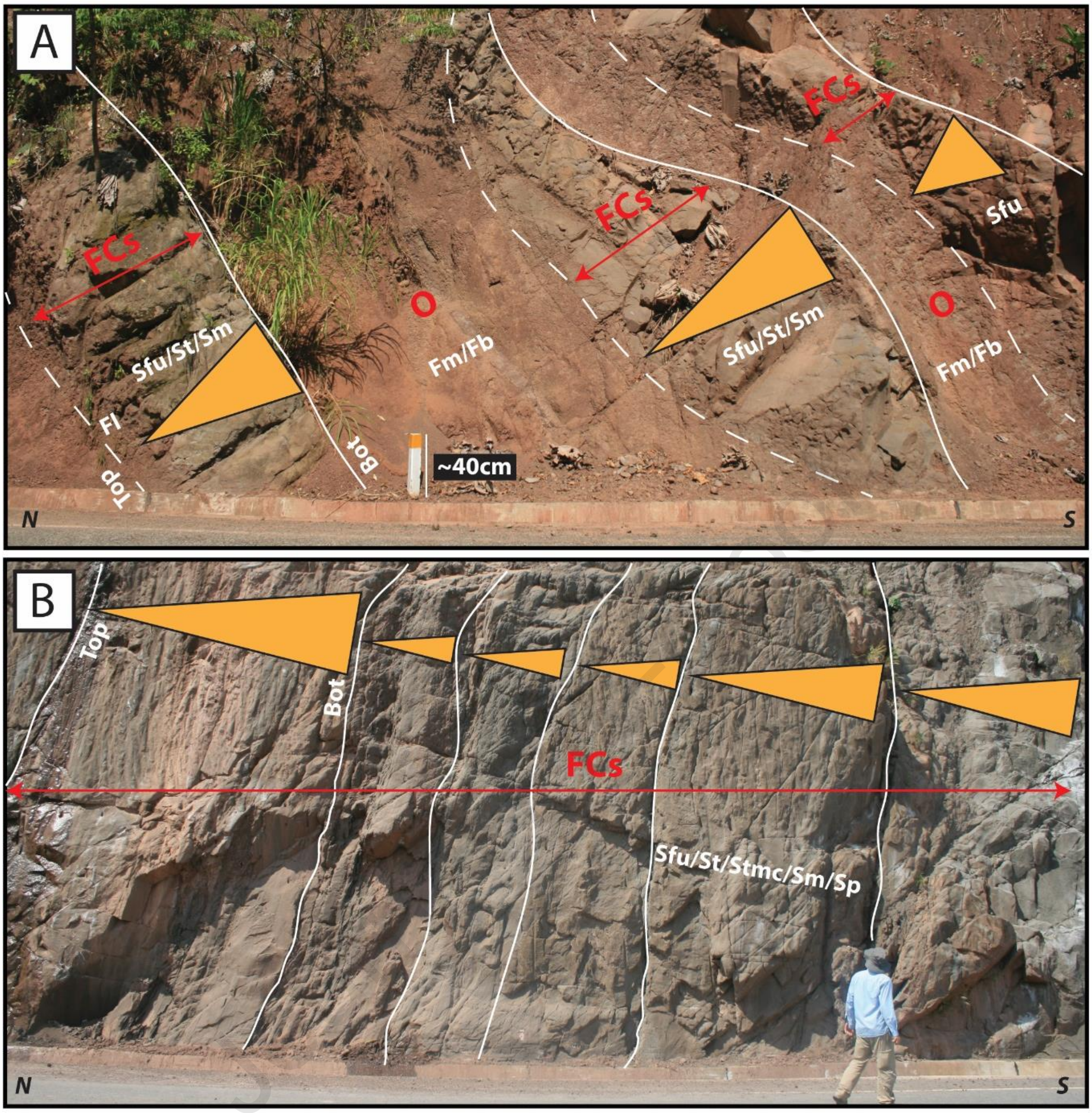

Figure 10. Two distinct vertical organizations (stacking) of alternating FCs and O facies associations. The Punquiri syncline's axis is located at the left in both images (towards the North and stratigraphic top). A) Outcrop MD 197 showing overturned strata. Isolated meter-thick and fining-upward fluvial channels (FCs) are separated by thick fine-grained overbank deposits (O). B) Outcrop MD 209 showing vertically stacked fluvial sandstones presenting a fining-upward pattern. Sandstones are mainly made up of facies Sfu, St, Stmc, Sm, and Sp. Because of the important thickness of facies association FCs (range between 10-15m), lower and upper contacts with facies association O are not visible here. Martin Roddaz for scale (1.76m).

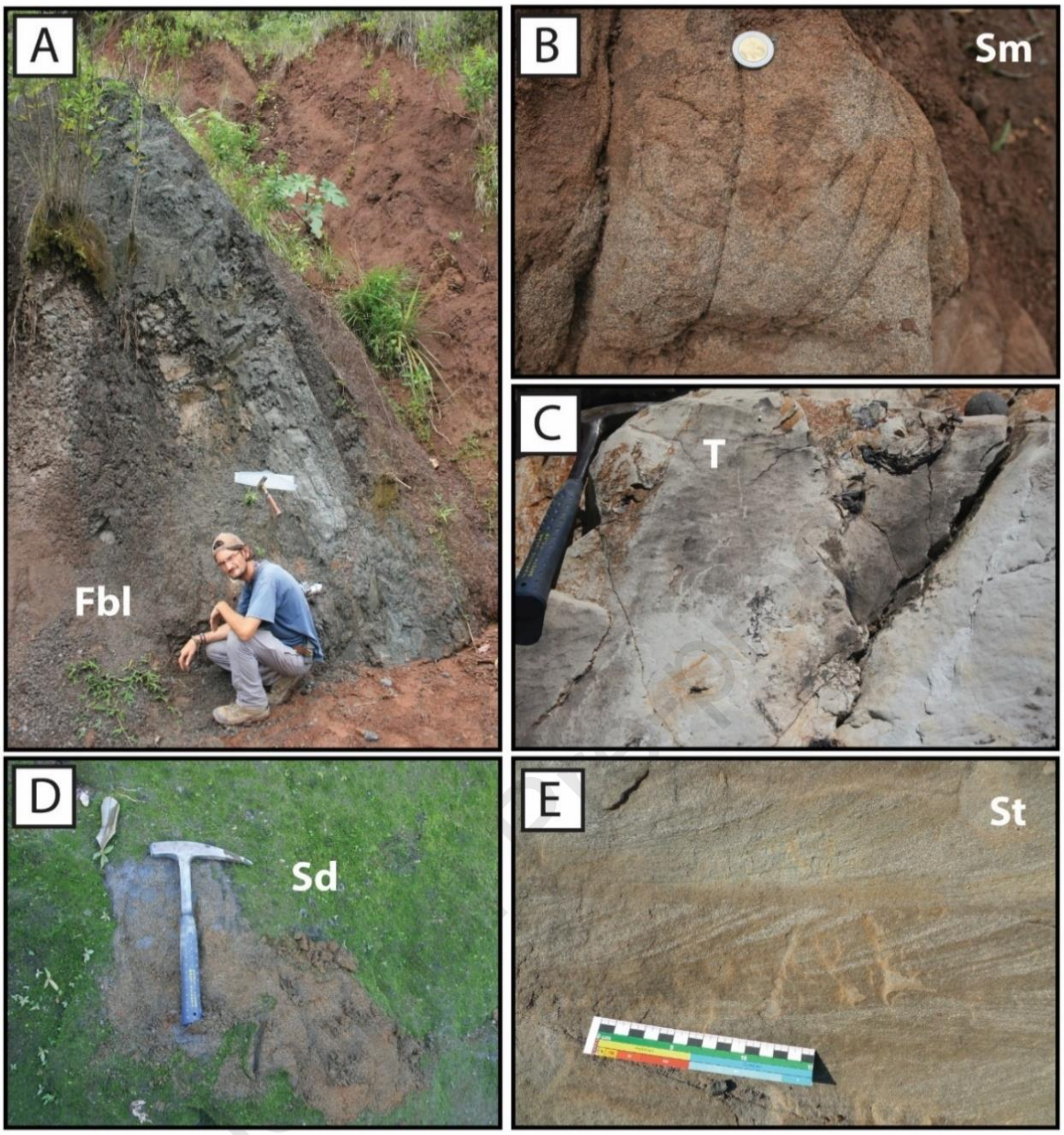

Figure 11. Examples of facies found in the Neogene of the Madre de Dios foreland basin. A) Facies Fbl showing grey mudstones to siltstones. B) Facies Sm showing structureless medium-grained massive sandstones. C) Facies T showing a tuffaceous rock with plant fragments and some ripples. D) Facies Sd showing shaly fine-grained sandstone E) Facies St showing trough cross-bedded in fine-to medium-grained sandstones.

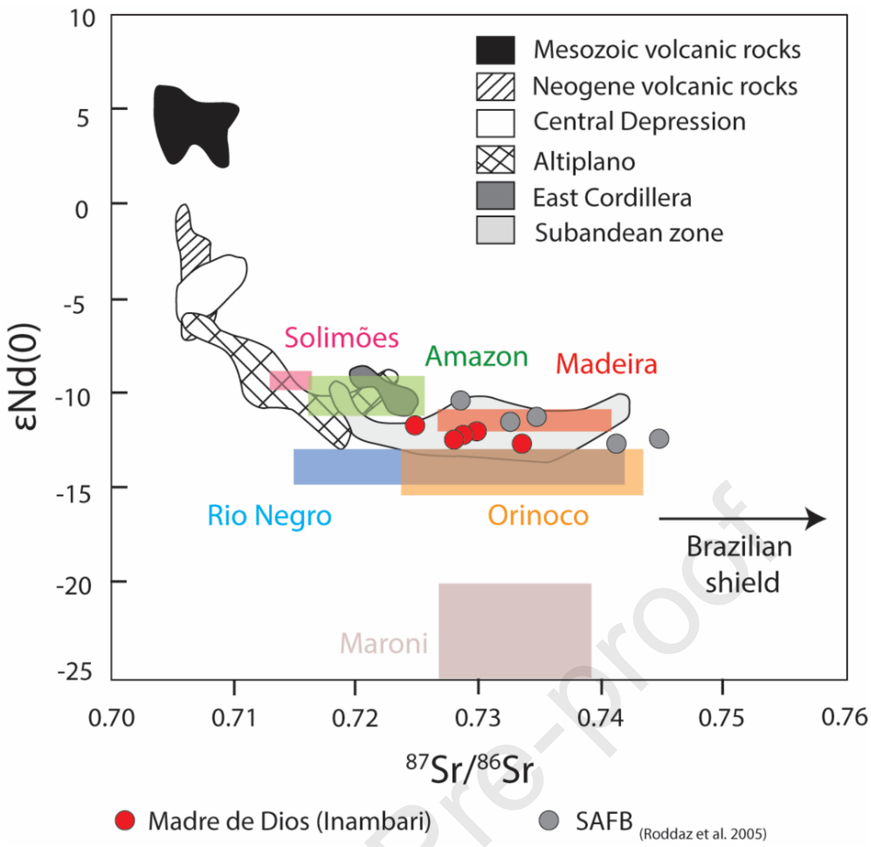

Figure 12. $^{87}Sr/^{86}Sr$-εNd (0) diagram for Neogene Madre de Dios foreland basin sedimentary rocks compared with several relevant source areas and modern suspended particulate material in western Amazonia. Quaternary Ecuadorian volcanic lavas are from Barragan (1998); the Mesozoic and Neogene volcanic rocks are from Kay and Rogers (1994) and Rogers; data for the Central depression, the Altiplano, the Eastern Cordillera, and the Subandean zone are taken from Pinto (2003) and Roddaz et al., (2005a). SPM from the Tapajós, Negro, Urucara, and Trompetas (Allègre et al., 1996), Madeira and Solimões rivers (Viers et al., 2008) and the Amazon, Orinoco, and Maroni rivers (Rousseau et al., 2019).

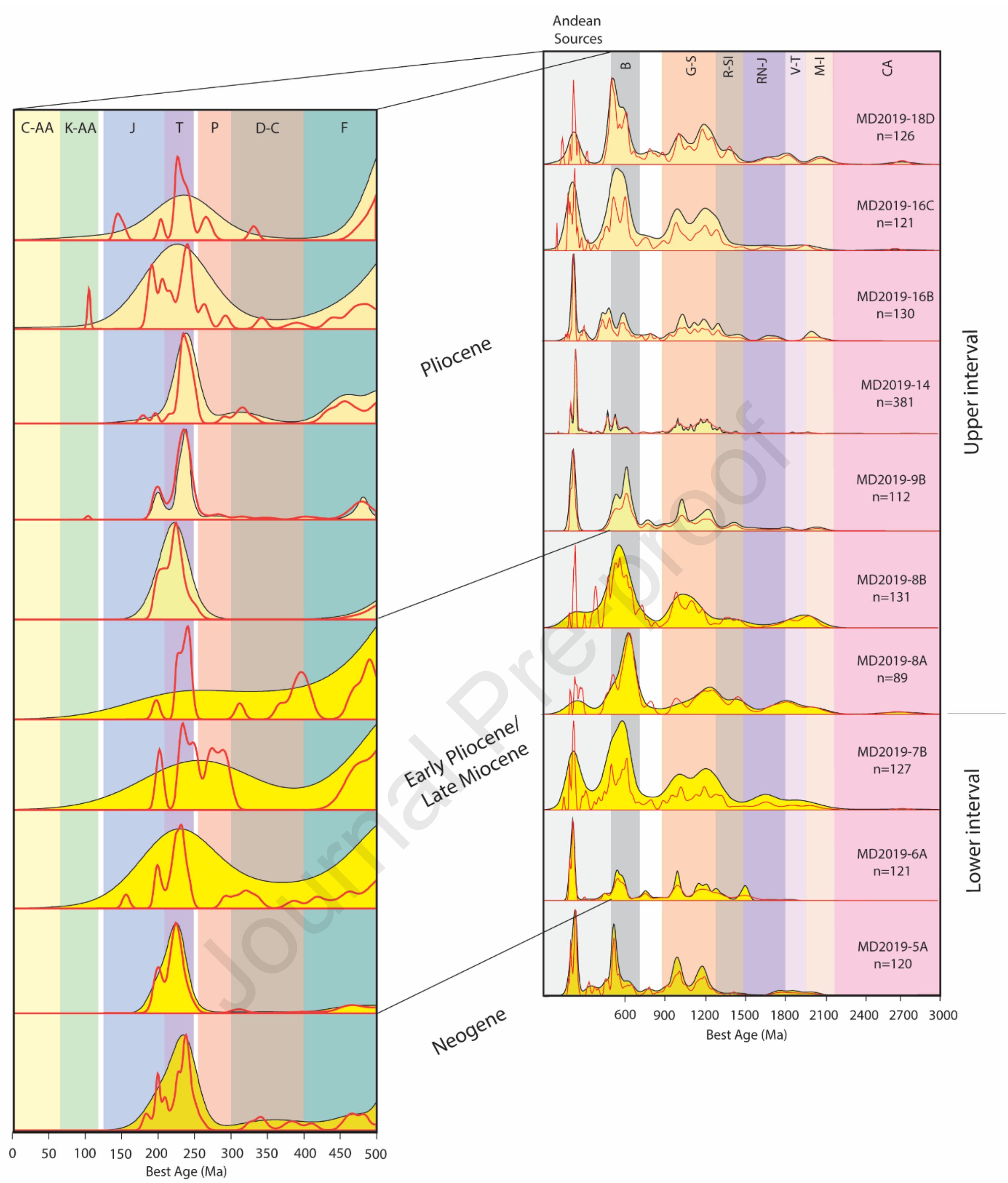

Figure 13. Stratigraphic evolution of U-Pb ages on zircon grains with age distributions displayed by their Kernel Density Estimation (KDE) and Probability Density Plots (PDP; red line). C-AA: Cenozoic Andean Arc (Less than 60 Ma); K-AA: Cretaceous Andean Arc (66-120 Ma); J: Jurassic Extension & Chocolate Arc (130-216 Ma); T: Triassic rift (216-250 Ma); P: Permian magmatism (252-290 Ma); D-C: Devonian & Carboniferous magmatism (300-400 Ma); F: Famatinian (400-500 Ma); B: Brasiliano (500-700 Ma); G-S: Greenville-Sunsás (900-1300 Ma); R-SI: Rondonia-San Ignácio (1300-1540 Ma);

RN-J: Rio Negro-Juruena (1540-1820 Ma); V-T: Ventuari-Tapajós (1820-2000 Ma); M-I: Maroni-Itacaiunas (2000-2200 Ma); CA: Central Amazon (>2200 Ma). Age ranges are from Tassinari et al. (2000), Reimann et al. (2010), and Chavez et al. (2022).

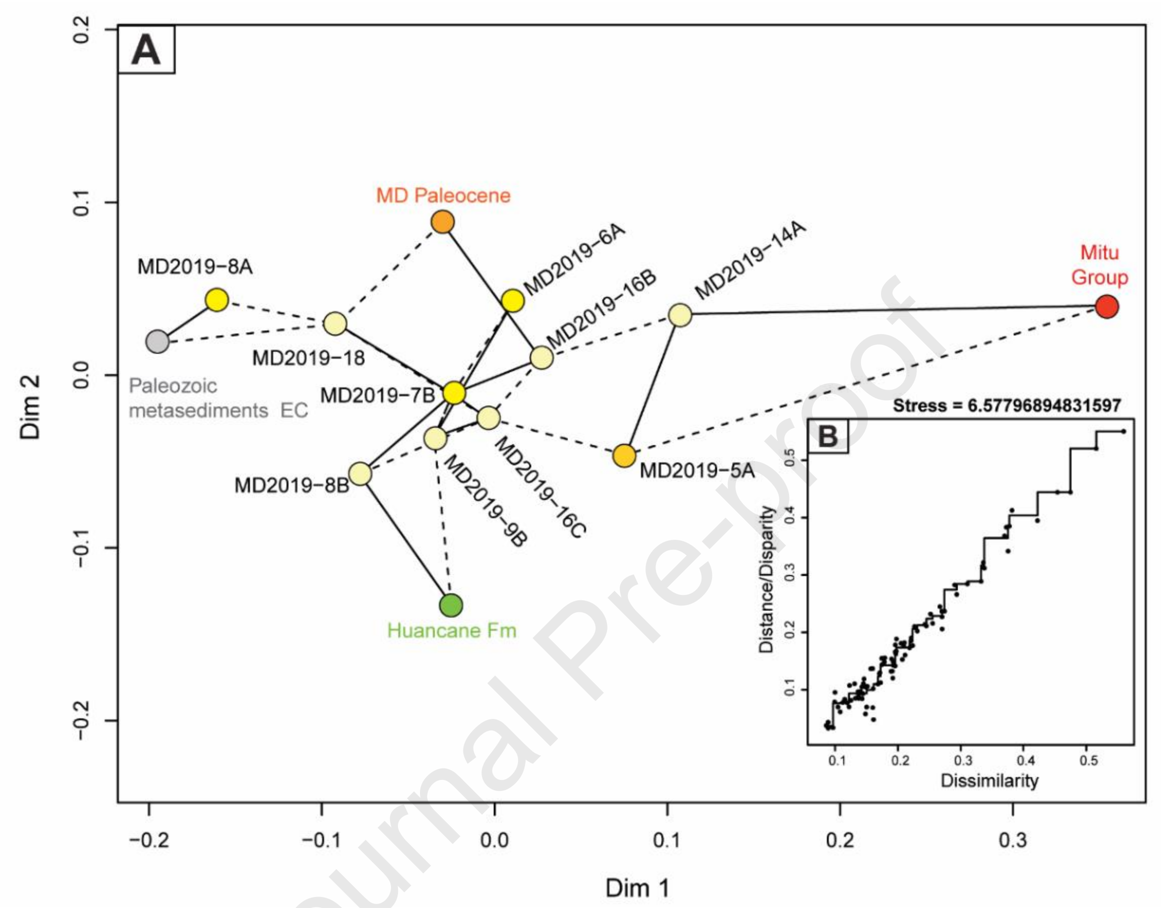

Figure 14. A) MDS map based on the U-Pb age distributions of detrital zircons grains using the Kolmogorov-Smirnov test. The closest and second closest neighbors are linked by solid and dashed lines, respectively. Data for MD Paleocene (combination of samples MD85, 176, 177, 239, 255, and 256) can be found in Louterbach et al. (2018b); Mitu Group, Triassic magmatic rocks, and Huancané formation are from Spikings et al. (2016). Paleozoic metasedimentary rocks EC consist of the combination of the metasedimentary rocks analyzed in Reiman et al (2010) and Bahlburg et al. (2011). B) Sherpard plot of the U-Pb data showing the transformation from dissimilarity to distances and disparities (Vermesch, 2013).

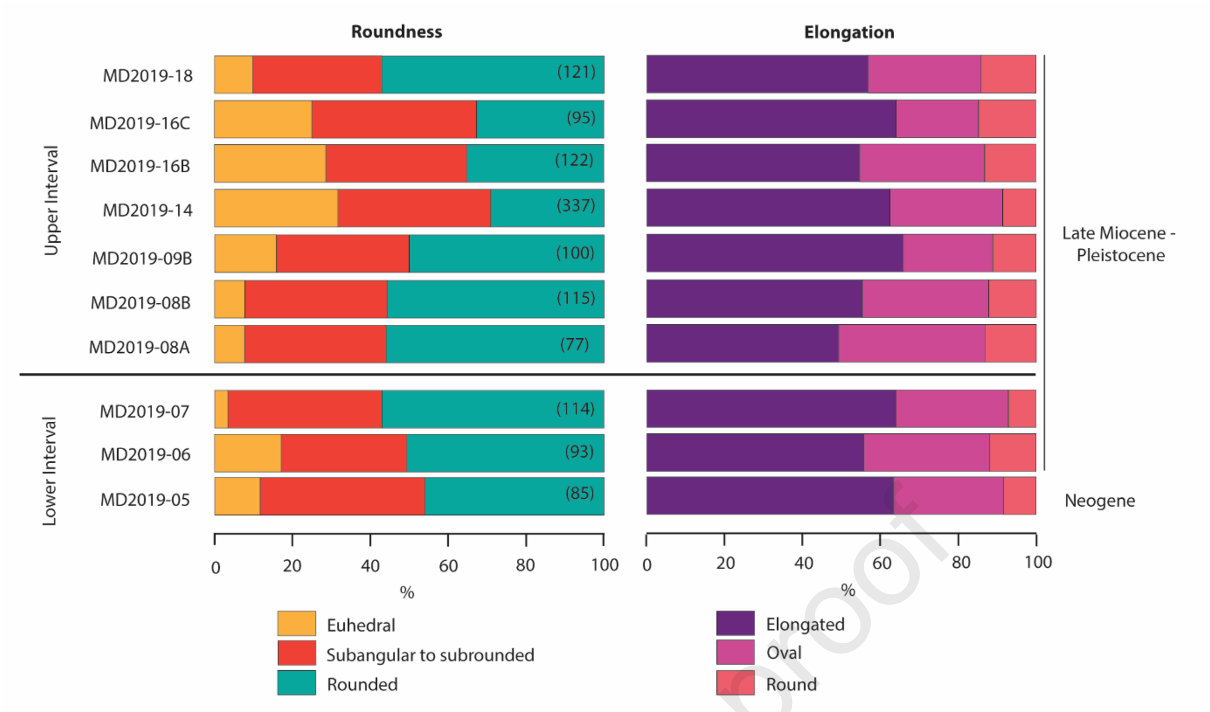

Figure 15. Roundness and elongation for detrital zircons with concordant ages. Broken grains without a clear shape in the BSE images were not included.

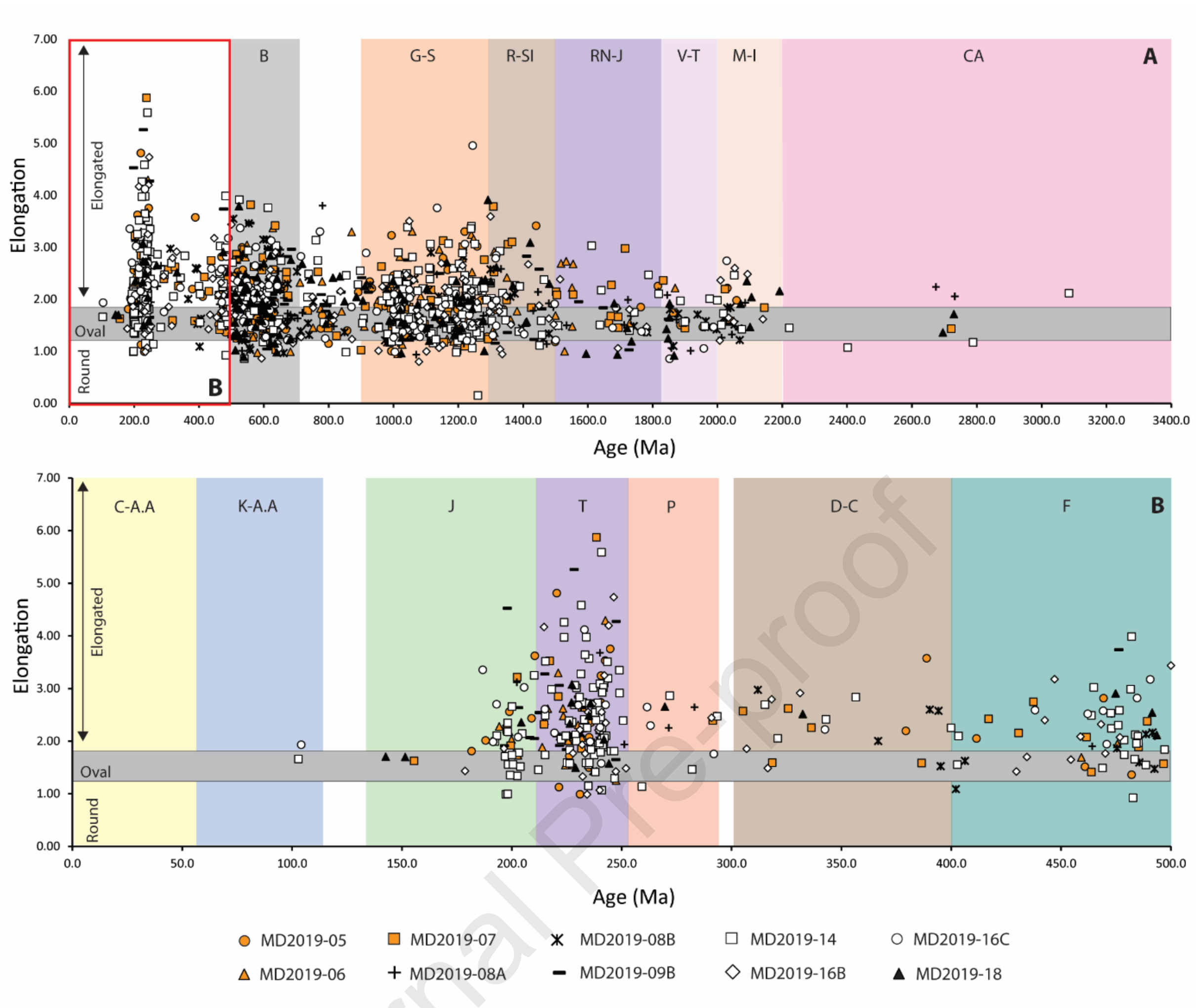

Figure 16. Detrital zircon shape vs. concordant age. The field for oval grains (length/width=1.3/1.8) is marked by a horizontal gray bar. **A)** Plot covering all the ages observed. **B)** Close-up on detrital zircon ages younger than 500 Ma, characteristics of Andean provenance.

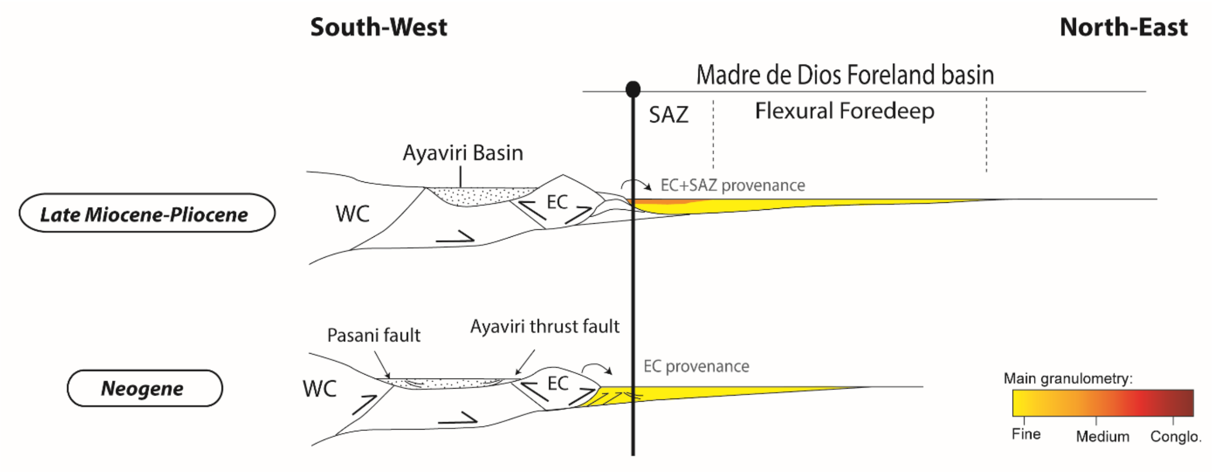

Figure 17. Sketch showing the evolution of the Southern Amazonian retro arc foreland basin system from the Early Miocene to the present day. The black line indicates the approximate location of the studied area. Early Miocene activities and related growth strata of the Pasani and Ayaviri thrust faults are reported in Perez and Horton (2014). WC: Western Cordillera; EC: Eastern Cordillera; SAZ: Sub-Andean Zone. Modified from DeCelles and Horton (2003). See text for details.

Highlights

- Timing of Late Miocene-Pliocene uplift of the Eastern Cordillera and Sub Andean Zone constrained by AFT and AHe data.
- Transition from a low to high energy fluvial system in the Late Miocene-Pliocene
- Provenance analysis of the Madre de Dios basin indicates Eastern Cordillera denudation and recycling of SAZ sediments.

Declaration of interests

☒ The authors declare that they have no known competing financial interests or personal relationships that could have appeared to influence the work reported in this paper.

☐The authors declare the following financial interests/personal relationships which may be considered as potential competing interests: